

Modelling large plastic deformations of cohesive soils using sequential limit analysis

D. Kong, C. M. Martin*, B. W. Byrne

Department of Engineering Science, University of Oxford, Parks Road, Oxford OX1 3PJ, UK

SUMMARY

This paper introduces sequential limit analysis (SLA) as a method for modelling large plastic deformations of purely cohesive materials such as undrained clay. The method involves solving a series of consecutive small-deformation plastic collapse problems using finite element limit analysis, thus ensuring high levels of accuracy, efficiency and robustness. The techniques needed to develop an SLA implementation for 2D (plane strain) problems are described in detail, including model geometry updating routines, treatment of rigid bodies, interfaces and boundaries, and periodic remeshing and interpolation of field variables. A simple total stress-based constitutive model is employed to account for strain softening and strain rate effects. Extensive verifications and validations are performed using analytical solutions and physical model test results, comparing both collapse loads and failure mechanisms, to demonstrate the effectiveness of the SLA approach. Additional solution quality checks on the bracketing discrepancy between lower bound and upper bound limit analysis solutions, and on the incompressibility of the rigid–plastic material, are also presented.

Copyright © 2016 John Wiley & Sons, Ltd.

Received ...

KEY WORDS: Numerical modelling; limit analysis; large deformation; remeshing; clay; pipeline

*Correspondence to: Department of Engineering Science, University of Oxford, Parks Road, Oxford OX1 3PJ, UK

†Please ensure that you use the most up to date class file, available from the NAG Home Page at

<http://www3.interscience.wiley.com/journal/3312/home>

1. INTRODUCTION

1.1. Background to sequential limit analysis

The foundations of limit analysis for perfectly plastic structures are the lower bound (LB) and upper bound (UB) theorems of plasticity [1, 2]. Together these theorems allow the exact collapse load for the structure to be bracketed in a rigorous manner. When limit analysis is applied to 2D or 3D continua, exact solutions can only be obtained for certain simple problems. In general it is necessary to obtain non-coincident LB and UB solutions numerically, either using bespoke stress and velocity fields (e.g. [3, 4, 5, 6]) or via finite element limit analysis (FELA). Most of the early implementations of FELA relied on linear programming optimisation techniques, which required the yield function to be linearised (e.g. [7, 8, 9, 10, 11]). More recent FELA implementations have tended to employ non-linear programming (e.g. [12, 13, 14, 15, 16, 17]) or conic programming (e.g. [18, 19, 20, 21, 22, 23]) optimisation techniques. These allow a range of smooth and non-smooth yield functions to be treated natively, without linearisation.

The instantaneous velocity field (or failure mechanism) of a skeletal structure or continuum region undergoing plastic deformation can be obtained from a UB solution for a given configuration of the model. The velocities can be integrated over a small time increment to yield a displacement increment, which in turn can be used to update the configuration of the deforming structure. A subsequent UB problem is then solved for the updated configuration. By repeating this process numerous times, a large-deformation problem can be solved by performing a sequence of small-deformation UB limit analyses. This is the so-called sequential limit analysis (SLA) method, first introduced for large plastic deformations of planar truss and frame structures by Yang [24]. Recent progress in computational limit analysis using FELA has opened up the possibility of applying the SLA technique to more complex problems involving large plastic deformations. For problems involving a plastically deforming continuum region, remeshing of the deforming domain can be performed as often as necessary to preserve the FELA solution accuracy and to avoid mesh distortion. Softening or hardening behaviour of the material, as well as viscous rate effects, can

1 be accounted for by updating the distribution of local material strengths used for each incremental
 2 UB analysis.

3 It was shown in [24] that SLA can achieve reliable geometric updating even with much larger time
 4 increments than those typically used in large-deformation finite element (FE) analysis, significantly
 5 improving the computational efficiency. Moreover, as will be shown in this paper, SLA has an
 6 advantage over large-deformation FE analysis of being highly stable under material and geometrical
 7 nonlinearities, since no updating or interpolation of the stress field is required during the simulation.
 8 It is important to note that successful application of the SLA approach has previously been confined
 9 to relatively simple structural problems such as frames and plates, where contact and interface
 10 conditions are not relevant [24, 25, 26]. To extend this method for the study of continuum problems,
 11 the interfaces and external boundaries of the model have to be treated carefully. In addition, practical
 12 applications involving continua frequently require consideration of the effects of strain softening and
 13 strain rate on the material strength.

14 The SLA approach described here uses the in-house FELA code OxLim [18, 19, 21, 27],
 15 with Triangle [28] for 2D unstructured mesh generation and ParaView [29] for visualisation.
 16 In an OxLim analysis, the application of the LB and UB theorems to a continuum region
 17 (discretised into triangular finite elements) leads to two separate second-order cone programming
 18 problems that are optimised using the commercial software MOSEK [30]. In the LB/UB analyses,
 19 statically/kinematically admissible discontinuities are incorporated between elements to yield
 20 more satisfactory solutions than those obtainable from fully continuous stress/velocity fields. In
 21 principle, only UB analyses are needed for SLA modelling because each analysis increment
 22 involves geometric updating using just the computed velocity field. However, LB analyses can also
 23 be performed simultaneously in order to assess the accuracy of the computed UB solutions, by
 24 monitoring the gap between the bounds. A schematic overview of the SLA method employed here
 25 is shown in Figure 1. The whole process is automatically controlled by code written in Python.

1.2. Application to geotechnical problems

When applying SLA to geotechnical problems involving large plastic deformations of cohesive soils such as undrained clay, certain behaviours of the soil such as elastic response and consolidation cannot be considered directly. Additionally, the velocity field obtained from a UB analysis using FELA is not exact; instead a numerical optimisation problem is solved approximately, to a finite tolerance, for a particular mesh discretisation. Over a sequence of such analyses, particularly when there is remeshing at regular intervals, it is inevitable that some numerical error will accumulate. Nevertheless, SLA can provide the most important information (collapse load and failure mechanism) at a fraction of the cost of conventional incremental FE methods, making it very attractive for large-deformation problems [24, 25]. To use SLA for practical applications it is of course necessary that the deforming material can be reasonably idealised as rigid-plastic and obeying an associated flow rule, as required by the theorems of limit analysis.

A number of other advanced numerical approaches are available for the analysis of geotechnical problems involving large plastic deformations. These include the material point method [31, 32, 33, 34], smoothed particle hydrodynamics [35, 36, 37, 38] and the distinct element method [39, 40, 41, 42, 43, 44], though at present the most widely used approaches are FE-based methods such as the arbitrary Lagrangian-Eulerian (ALE) [45, 46], remeshing and interpolation technique with small strain (RITSS) [47, 48, 49, 50] and coupled Eulerian-Lagrangian (CEL) [51, 52, 53, 54, 55, 56, 57, 58] techniques. The RITSS method originally developed in [47] is an improved ALE approach which divides a large-deformation problem into a series of small-deformation FE analyses. It can be seen that in this respect, the SLA method introduced here is similar to the RITSS method, but each SLA increment involves solving one or two computational limit analysis problems (UB and optionally LB) rather than performing an increment of conventional elastic-plastic FE analysis.

Where large plastic deformations of cohesive soil are caused by an indenter, penetrometer or foundation element that can be treated as a rigid body, and where the elastic deformation of the soil is of little importance to the solution, the proposed SLA method could potentially be

1 more attractive than the other numerical approaches described above, considering the computing
 2 efficiency. However, the focus of this paper is on demonstrating that the use of SLA for such
 3 problems is satisfactorily accurate and efficient in its own right, rather than attempting to present
 4 detailed comparisons between SLA and other methods. In any case, objective comparisons are
 5 extremely difficult and impractical to achieve, as will be discussed in Section 4.2.

6 The techniques introduced in this paper for the treatment of rigid bodies can in principle be
 7 applied to any convex polygon, although, for the sake of simplicity, these polygons are represented
 8 by circles when schematic diagrams are provided. All of the examples studied here (plate, wedge,
 9 strip footing, pipe segment, etc.) are plane strain problems involving interactions between rigid
 10 bodies and undrained soil, which undergoes plastic deformation at constant volume. Although
 11 similar SLA simulations could readily be undertaken with cohesive-frictional or purely frictional
 12 materials, the assumption of associated flow (a requirement for any method based on classical limit
 13 analysis) leads to unrealistically high levels of dilation in such materials (see e.g. [19, 21, 22]), such
 14 that large deformations computed using SLA are unlikely to be of great practical value.

15 By employing an axisymmetric FELA solver, the present SLA approach could readily be adapted
 16 to analyse the vertical loading behaviour of rigid objects such as ball penetrometers or spudcan
 17 footings in cohesive soils. Moreover, gravity-driven problems without rigid bodies, such as slope
 18 stability (e.g. [19, 21, 27]) and tunnel face collapse (e.g. [59, 60]) could also potentially be solved
 19 using SLA to model progressive large plastic deformations. These problems are, however, not
 20 investigated here since the emphasis is on soil–structure interactions.

2. DEVELOPMENT OF MODELLING APPROACH

21 2.1. Updating of model geometry

22 At a given increment in an SLA simulation, the coordinates of an individual node are updated by

$$\vec{X} = \vec{x} + \vec{v} \cdot \Delta t \quad (1)$$

1 where \vec{x} and \vec{X} are the coordinates at the beginning and end of the increment, \vec{v} is the nodal velocity
 2 from the UB velocity field, and Δt is the incremental time step.

3 Because of the kinematically admissible velocity discontinuities employed in the UB analysis
 4 using OxLim, nodes on the external boundary of the model, see Figure 2, may require velocity
 5 averaging. This is illustrated in Figure 3, where an arbitrary node Q on the external boundary has
 6 several evaluation points sharing the same coordinates, but having different velocity vectors. Three
 7 types of external boundary node are recognised in Figure 2. Those on the free surface and not
 8 in contact with the rigid body are termed surface nodes; those in contact with the rigid body but
 9 adjacent to a surface node are termed margin nodes; and those between the two margin nodes are
 10 termed interface nodes. The velocity of a surface node is simply determined as the average of the
 11 velocity vectors corresponding to all of its evaluation points, and the nodal displacement is updated
 12 accordingly using Equation 1. The positions of the interface nodes can be conveniently reconstructed
 13 at each increment using the coordinates of the rigid body vertices, based on the assumption that
 14 no separation occurs within the contact domain between the two margin nodes. The incremental
 15 evolution of the contact domain can be achieved by tracking the positions of the margin nodes
 16 relative to the rigid body; this procedure is explained below.

17 *2.1.1. Velocity of a margin node* After the UB velocity field has been obtained, each margin node
 18 is checked to see whether it moves tangentially along the rigid body segment to which it is currently
 19 adjacent, hereafter referred to as a margin segment. If it does not (this is possible when a no-tension
 20 interface condition has been prescribed) then the node breaks away from the rigid body. In the
 21 present SLA implementation, the criterion used to check whether a node moves along a rigid body
 22 segment requires at least one evaluation point satisfying

$$\cos \theta = \frac{\|(\vec{v}_{(i)} - \vec{v}_r) \cdot \vec{s}\|}{\|\vec{v}_{(i)} - \vec{v}_r\| \cdot \|\vec{s}\|} \geq \cos \theta_{cri} \quad (2)$$

23 where $\|\cdot\|$ denotes the Euclidean norm of a vector, $\vec{v}_{(i)}$ is the velocity of the i th evaluation point,
 24 \vec{v}_r is the velocity of the rigid body and \vec{s} is the vector of the rigid body segment determined by the

1 coordinates of its two endpoints. θ is the angle between $(\vec{v}_{(i)} - \vec{v}_r)$ and \vec{s} , and θ_{cri} is the tolerance of
 2 θ with a default value of 10^{-4} rad.

3 If Equation 2 is not satisfied for any evaluation point associated with the margin node, the node
 4 is concluded to have broken away from the rigid body, and other nodes in the contact domain near
 5 it are checked consecutively as illustrated in Figure 4a, until an end node $n_{(e)}$ satisfying Equation 2
 6 is found. After that, the nodes $n_{(0)}$ to $n_{(e-1)}$ are released from the contact boundary and updated as
 7 surface nodes, while node $n_{(e)}$ is updated as the new margin node (see Figure 4b) and its velocity
 8 \vec{v}_{mar} is determined as

$$\vec{v}_{mar} = \frac{\sum \|(\vec{v}_{(i)} - \vec{v}_r) \cdot \vec{s}\|}{l \cdot \|\vec{s}\|} \cdot \frac{\vec{s}}{\|\vec{s}\|} + \vec{v}_r \quad (3)$$

9 where l is the total number of evaluation points associated with the margin node, which depends on
 10 the local connectivity. This determination of \vec{v}_{mar} ensures that the direction of $(\vec{v}_{mar} - \vec{v}_r)$ coincides
 11 with that of \vec{s} , and that all the components of $(\vec{v}_{(i)} - \vec{v}_r)$ along \vec{s} are averaged.

12 *2.1.2. Coordinate update of a margin node* In an OxLim analysis, the kinematical constraints
 13 associated with rigid body motion are only applied where a rigid body is in contact with the material
 14 of the rigid-plastic continuum. Therefore, any segments of a rigid body that are not currently in
 15 contact with the material are not included in the analysis. Consequently, the OxLim UB results
 16 can provide information on whether a margin node moves tangentially along the current margin
 17 segment, but not on whether a new rigid body segment will be involved in subsequent increments.

18 In the SLA modelling performed here, a rigid body is assumed to be a convex polygon with
 19 N segments/vertices, each of which is assigned an index j (varying from 0 to $N - 1$) denoting its
 20 position in the segment/vertex list of the body. An arbitrary segment $S_{(j)}$ is formed by two vertices
 21 $P_{(j)}$ and $P_{(j+1)}$. Since the rigid body is closed, $j + 1$ should be replaced by 0 if $j = N - 1$. After the
 22 velocity of the margin node, \vec{v}_{mar} , has been determined as described above, the vertex that the node
 23 moves towards is deduced to be $P_{(m+k)}$, where m is the index of the margin segment $S_{(m)}$, and k is
 24 given by

$$k = \max(0, \text{sign}[(\vec{v}_{mar} - \vec{v}_r) \cdot \vec{s}_{(m)}]) = 0 \text{ or } 1 \quad (4)$$

1 where $\vec{s}_{(m)}$ is the vector of the margin segment $S_{(m)}$ (vertices $P_{(m)} \rightarrow P_{(m+1)}$). The time dt that would
 2 be required for the margin node to move to reach and coincide with $P_{(m+k)}$ is calculated as

$$dt = \frac{\|\vec{x}_{(m+k)} - \vec{x}_{mar}\|}{\|\vec{v}_{mar} - \vec{v}_r\|} \quad (5)$$

3 where $\vec{x}_{(m+k)}$ and \vec{x}_{mar} are the coordinates of $P_{(m+k)}$ and the margin node respectively. The time step
 4 Δt used to update the model geometry is then determined as

$$\Delta t = \min(dt, \Delta t_{lim}) \quad (6)$$

5 where Δt_{lim} is a limiting incremental time step set by the user. If Δt_{lim} is chosen to update the nodal
 6 coordinates, the margin node will remain on $S_{(m)}$, though at a different intermediate position. If dt
 7 is chosen, the node will move to coincide with $P_{(m+k)}$, which is exactly at the corner formed by
 8 segments $S_{(m)}$ and $S_{(m+h)}$, where $S_{(m+h)}$ is the potential segment that the node moves towards, with
 9 h given by

$$h = \text{sign}[(\vec{v}_{mar} - \vec{v}_r) \cdot \vec{s}_{(m)}] = \pm 1 \quad (7)$$

10 To carry on the analysis, the margin node is now forced to ‘jump’ by a very short distance onto
 11 $S_{(m+h)}$ to reflect the existence of this new segment in the subsequent OxLim analysis. The final
 12 coordinates of the margin node, denoted by \vec{X}_{mar} , are determined as

$$\vec{X}_{mar} = \vec{X}_{(m+k)} + \zeta \cdot h \cdot (\vec{X}_{(m+1+h)} - \vec{X}_{(m+h)}) \quad (8)$$

13 where $\vec{X}_{(m+1+h)}$ and $\vec{X}_{(m+h)}$ are the coordinates of $P_{(m+1+h)}$ and $P_{(m+h)}$ at the end of the increment,
 14 and ζ is a fraction parameter, which should be small (relative to 1) to avoid spurious modification
 15 of the model configuration; for this paper a value of 0.05 is used.

16 Figure 5 shows a schematic of how this operation is performed, where $h = +1$ is assumed. This
 17 operation is performed to notify OxLim that a new margin segment will be involved in the next
 18 increment, however it does not necessarily force the margin node to move along this segment in the
 19 next increment (it may break away).

20 **2.1.3. Inter-penetration of material into a rigid body** After the nodal coordinates have been
 21 updated, it is possible that some nodes on the free surface(s) near a rigid body encroach into it.

1 To check whether an arbitrary node, n , is within a convex domain, all N vertices, from $P_{(0)}$ to
 2 $P_{(N-1)}$, of this domain are sorted in counterclockwise order, as illustrated in Figure 6. For each
 3 vertex, a vector $\vec{v}_{(j)}$ is then defined as the cross product of the vectors $n \rightarrow P_{(j)}$ and $P_{(j)} \rightarrow P_{(j+1)}$,
 4 which are illustrated in Figure 6. The index $j + 1$ should be replaced by 0 when $j = N - 1$. Node n
 5 is determined to be within the convex domain if

$$\text{sign}[\vec{v}_{(j)}] > 0 \quad \forall j \in \{0, \dots, N - 1\} \quad (9)$$

6 The surface nodes need to be checked for inter-penetration consecutively in the order from the
 7 margin node working towards the free surface (see Figure 7a). Of all the nodes that have encroached,
 8 the one at the end of the search is recognised as $n_{(e)}$, where e is an index denoting its position in
 9 the list. The nodes from $n_{(1)}$ to $n_{(e)}$ are then projected perpendicularly onto the nearest rigid body
 10 segment, and additional contact is thus enforced (see Figure 7b). Node $n_{(e)}$ is then updated as the
 11 new margin node n_{mar} , while nodes $n_{(0)}$ to $n_{(e-1)}$ are updated as interface nodes.

12 *2.1.4. Self-contact behaviour* Possible self-contact of a free surface, where surface nodes encroach
 13 into the boundary formed by the surface itself, as illustrated in Figure 8a, must also be addressed. As
 14 described above, a free surface in the present SLA implementation comprises a list of nodes (and
 15 segments), sorted in consecutive order from the margin node working outwards. Each node (and
 16 segment) has an index representing its position in the corresponding list.

17 After the model geometry has been updated in an SLA increment, free surface segments are
 18 checked to ensure that preceding segments do not intersect them, e.g. in Figure 8a, segments $S_{(0)}$ to
 19 $S_{(p-1)}$ are checked to find any that intersect with segment $S_{(p)}$ (end points $n_{(p)}$ and $n_{(p+1)}$). If several
 20 segments are found to intersect with $S_{(p)}$, the one with the smallest index number is recognised as
 21 $S_{(q)}$ (see Figure 8a). A new node n_s (see Figure 8b) is then generated at the intersection point, after
 22 which all the nodes from $n_{(q+1)}$ to $n_{(p)}$ are removed from the free surface node list, while n_s is
 23 inserted in the new node list immediately after $n_{(q)}$. A new segment list is then generated and the
 24 surface is reconstructed accordingly, as shown in Figure 8b. A similar operation is performed on the
 25 reconstructed surface, and this is repeated until all self-intersections have been handled.

2.2. Strain softening and strain rate

A modified Tresca soil model proposed by Einav and Randolph [61] is employed in the SLA simulations to account for the effects of strain softening and strain rate:

$$s_u = s_{u0} \times [\delta_{rem} + (1 - \delta_{rem})e^{-3\xi/\xi_{95}}] \times [1 + \mu \log_{10}(\frac{\max(\dot{\gamma}, \dot{\gamma}_{ref})}{\dot{\gamma}_{ref}})] \quad (10)$$

where s_{u0} denotes the intact undrained shear strength of the soil, the first bracketed term accounts for softening behaviour as a function of the accumulated plastic shear strain, ξ , while the second bracketed term accounts for viscous rate effects as a function of the current maximum shear strain rate, $\dot{\gamma}$, at the material point in question. The softening parameter δ_{rem} is the ratio of the fully remoulded shear strength to the initial shear strength of the soil (i.e. the inverse of the sensitivity, S_t). The ductility parameter ξ_{95} corresponds to the plastic shear strain at which the soil has undergone 95% of the reduction in strength due to remoulding. For typical soft marine clays, S_t ranges from 2 to 5 and ξ_{95} ranges from 10 to 50 [62]. The reference shear strain rate $\dot{\gamma}_{ref}$ is usually taken as 3×10^{-6} /s, approximately 0.01/h [42]. The viscosity parameter μ represents the rate of strength increase per decade of strain rate increase, and is typically in the range 0.05 to 0.2 for cohesive soils [63, 64]. The maximum shear strain rate $\dot{\gamma}$ is defined as the difference between the major and minor principal strain rates.

In Equation 10, the parameters δ_{rem} , ξ_{95} , μ and $\dot{\gamma}_{ref}$ are considered to be constant soil properties and are not updated during the analysis. The parameters s_{u0} and ξ serve as history variables at material points, and interpolations are conducted to obtain their values at the beginning of each increment if remeshing is performed. The values of the maximum shear strain rate $\dot{\gamma}$ calculated from the UB velocity field are discontinuous between elements. Therefore, $\dot{\gamma}$ at a node is obtained using an inverse distance weighting function [47], as

$$\dot{\gamma} = \frac{\sum \dot{\gamma}_{(i)} \cdot d_{(i)}^{-a}}{\sum d_{(i)}^{-a}} \quad (11)$$

in which $\dot{\gamma}_{(i)}$ is the maximum shear strain rate at the centroid of the i th element connected to the node, d_i is the distance between the node and the centroid of the i th element, and a is an exponent taken to be 3.5 as suggested by Hu and Randolph [47] and TECPLOT [65]. At the end of an increment,

1 the accumulated plastic shear strain at each node is updated as

$$\xi_{(t+\Delta t)} = \xi_{(t)} + \dot{\gamma} \cdot \Delta t \quad (12)$$

2 With the variables described above, the operative shear strength at each node of the SLA model
 3 can be calculated. A linear variation of strength within each triangular element is obtained by
 4 prescribing separate strengths at each vertex. Although second-order triangular elements are used
 5 for interpolation of field variables, as described below, the information carried by the mid-side nodes
 6 is not used for determining the operative strength distribution, as a quadratic variation of strength
 7 within each element is not currently handled by OxLim.

8 2.3. Remeshing and interpolation

9 After the model configuration has been updated in each increment, the mesh is checked to see if any
 10 triangular element has an angle smaller than 20° . If so, remeshing is performed to avoid excessive
 11 mesh distortion. Remeshing is also required if there is a breakaway of interface nodes from a rigid
 12 body, a margin node 'jump', or encroachment of surface nodes into a rigid body. Apart from the
 13 localised corrections described in Sections 2.1.2 to 2.1.4, the model at the beginning of the $(n+1)$ th
 14 increment has the same configuration as that at the end of the n th increment. Thus the new meshed
 15 domain and the old one overlap, and are here referred to as the target plane and the reference plane,
 16 respectively, for interpolation of field variables. In the mapping step, all nodes of the target plane
 17 are first located in the elements of the reference plane, then the field variables are interpolated
 18 quadratically. To determine if a given node is located inside a particular element, the same strategy
 19 introduced in Section 2.1.3 is used (see Figure 6 and Equation 9).

20 Before conducting the n th analysis increment, a temporary coarse mesh $CM_{(n)}$ is generated. This
 21 mesh is then refined to ensure reliability of the field variable interpolation, as well as accuracy of the
 22 FELA solutions (LB and UB), for the particular increment. Two key field variables, the accumulated
 23 shear strain ξ and the maximum shear strain rate $\dot{\gamma}$, are interpolated from the refined mesh of the
 24 last increment, $RM_{(n-1)}$, to the coarse mesh of the current increment, $CM_{(n)}$. To ensure that the
 25 region of mesh refinement is large enough, these attributes at $RM_{(n-2)}$ are also mapped to $CM_{(n)}$.

1 Although the reference plane of $\text{RM}_{(n-2)}$ does not necessarily overlap completely with the target
 2 plane of $\text{CM}_{(n)}$, it still provides useful information for most of the nodes. For each field variable, the
 3 larger of the two values obtained from $\text{RM}_{(n-2)}$ and $\text{RM}_{(n-1)}$ is chosen. At this stage the values of
 4 these attributes for each node do not have to be accurate since they are only providing information
 5 for refining the coarse mesh, rather than the actual update of material properties.

6 For an arbitrary triangular element in the coarse mesh, the target area A_{ref} used to refine this
 7 element when generating the new mesh is determined by a heuristic

$$A_{ref} = f(\xi, \dot{\gamma}, \delta_{rem}, \xi_{95}, D, A_{min}) \quad (13)$$

8 where f is a function that varies with the problem investigated and D is a characteristic length such
 9 as footing width or pipe diameter. The definition of f ensures that A_{ref} decreases with ξ as well as
 10 with $\dot{\gamma}$, so regions that are severely remoulded or experiencing intense shearing are discretised with a
 11 finer mesh. Here an example formulation of f is given, which was established based on preliminary
 12 analyses. For each triangle in $\text{CM}_{(n)}$, if the accumulated shear strain ξ is larger than 0.05, or if the
 13 corresponding softening factor (i.e. the first bracketed term in Equation 10) is smaller than 0.9, A_{ref}
 14 of this region is set to be no larger than $0.01D^2$. Concerning the effect of strain rate, another limiting
 15 value for A_{ref} is determined as

$$A_{ref} = A_{min} \cdot \frac{\dot{\gamma}_0}{\max(\dot{\gamma}, 0.1s^{-1})} \quad (14)$$

16 in which $\dot{\gamma}_0$ is the maximum value of $\dot{\gamma}$ for all the triangles in $\text{CM}_{(n)}$, and A_{min} is a minimum target
 17 element area set by the user. After the coarse mesh $\text{CM}_{(n)}$ has been refined to generate $\text{RM}_{(n)}$
 18 based on the distribution of A_{ref} throughout the model, the field variables are finally mapped from
 19 $\text{RM}_{(n-1)}$ to $\text{RM}_{(n)}$ using quadratic interpolation (six-noded triangles). Full details of the remeshing
 20 and interpolation procedure are given in [66].

3. NUMERICAL EXAMPLES

21 This section presents a benchmarking study of the SLA approach. Seven problems with gradually
 22 increasing complexity are analysed, as summarised in Table I. These problems are divided into

two categories. The first category (verification) involves four widely studied plane strain plasticity problems that have analytical solutions. These problems are examined to confirm the correct functioning of the SLA method and its implementation, as well as to provide guidance for choosing key parameters (e.g. minimum element size A_{min} and incremental displacement δd) in readiness for the study of more complex and realistic problems. The other category (validation) involves three transverse pipe–soil interaction problems with increasingly complicated geometry evolution and non-linear material behaviour, where physical modelling results are available for comparison.

In addition to comparisons with available analytical solutions and model test results, the normalised bracketing discrepancy between the LB and UB solutions during the SLA simulations, defined as $(UB - LB)/(UB + LB)$, is presented to further demonstrate the high quality of the results. For all problems that involve the evolution of plastically deforming free surfaces, the total volume of the deforming material is also monitored to check for incompressibility.

A detailed comparison of the SLA approach with the CEL analysis capability available in Abaqus [67] has been performed as part of the more extensive verification and validation programme in [66]. Selected CEL results are provided here for comparison, but the numerical details of the CEL models are omitted for the sake of brevity. The reader is referred to [66] for this information.

3.1. General features of SLA modelling

For all analyses in this paper concerning the vertical loading behaviour of a rigid body (wedge, strip footing or pipe) penetrating into undrained soil, the dimensions and boundary conditions of the SLA model are as illustrated in Figure 9. Symmetry is exploited, with only the right-hand half of the soil domain modelled. The half-width and depth of the domain are denoted by $B/2$ and h respectively. The bottom and right sides of the domain are fixed, while the left side is assigned a symmetric boundary condition. The top side of the domain is set as a free surface. The soil is modelled as a rigid–plastic Tresca material with initial undrained shear strength defined as $s_{u0} = s_{um} + \rho z$, where s_{um} is the shear strength at the mudline (original free surface), ρ is the strength gradient and z is the depth below the mudline. When applicable, Equation 10 is used to consider the effects of

1 strain softening and strain rate on the operative shear strength at a material point. For the modelling
 2 of ideal (i.e. perfectly plastic, rate-independent) soil in the first four examples, the sensitivity and
 3 viscosity parameters are set to $S_t = 1$ and $\mu = 0$.

4 The various rigid bodies used in the analyses are composed of straight-line segments (60 segments
 5 for the circular pipe). The rigid bodies are free to move in the vertical direction only, except in the
 6 final example where there is freedom in both the vertical and horizontal directions. In all cases
 7 rotation is prevented. At the interface between a rigid body and the soil, tension is not permitted to
 8 develop, and the limiting shear stress is defined as $\tau_{int} = \alpha s_u$, where α is the roughness coefficient
 9 for the interface and s_u is the operative shear strength of the adjacent soil. For the examples involving
 10 continuous penetration from the soil surface, the invert (lowest point) of the rigid body is initially
 11 positioned at a depth of $0.001D$. The vertical resistance experienced by the rigid body during
 12 penetration is denoted by V_c , and the vertical displacement is denoted by d . For the SLA results
 13 presented later, the resistances are taken as the average of the LB and UB solutions, while the
 14 failure mechanisms are only from the UB solution.

15 In all examples, the minimum target element size in the mesh is denoted by A_{min} , and the rigid
 16 body displacement used for each incremental analysis of the SLA process is denoted by δd .

17 3.2. Vertical loading of a buried plate

18 The undrained bearing capacity of a deeply buried rough thin plate, assuming conditions of plane
 19 strain, was studied analytically by Rowe and Davis [68] using slip-line theory. In the SLA analyses
 20 the plate (of half-width $D/2$) was modelled with a thickness of $0.02D$, and was initially embedded at
 21 a depth of $2D$ below a fixed surface. The dimensions $B/2$ and h of the soil domain were $3D$ and $5D$
 22 respectively. The plate was displaced vertically downwards by $1D$ using increments of $\delta d = 0.005D$.
 23 Four values of the minimum element size, A_{min} , were considered: 0.001 , 0.002 , 0.005 and 0.01 times
 24 D^2 .

25 Figure 10a shows the vertical load–displacement response of the plate. For the finest mesh, with
 26 $A_{min} = 0.001D^2$, a normalised resistance V_c/Ds_u of about 11.46 can be observed throughout the

large displacement of the plate. This value is only slightly higher than the analytical solution of $2 + 3\pi = 11.42$ derived in [68] for a plate with zero thickness. A rough-sided plate with a thickness of $0.02D$, as used here, would be expected to yield an additional normalised resistance component of 0.04 , so that the calculated result is very close to the analytical value. The normalised bracketing discrepancy between the LB and UB solutions decreases with mesh refinement as shown in Figure 10b, and is limited to about 1.5% for the mesh with $A_{min} = 0.001D^2$.

Figure 11 shows the soil failure mechanisms at the initial and final stages of loading. The shear strain rates $\dot{\gamma}$ are normalised using the plate width D and plate velocity v_p . The failure mechanisms are found to be identical at the different stages of loading, with the region of intense shearing contained entirely within the finely meshed area throughout the analysis. This confirms the effectiveness of the remeshing strategy described in Section 2.3.

3.3. Vertical loading of a buried pipe

Large vertical displacement of a deeply buried pipe is studied in this section. Analytical solutions for this problem are derived in [3] and [4], giving normalised resistance values of 9.20 (upper bound) for a smooth pipe and 11.94 (exact) for a rough pipe. In the SLA modelling, a rigid pipe cross-section of diameter D was pre-embedded with its invert at a depth of $3D$ below a fixed surface, and then displaced downwards by $1D$. The displacement increment δd and minimum element size A_{min} were chosen to be $0.005D$ and $0.001D^2$ respectively. Both smooth ($\alpha = 0$) and rough ($\alpha = 1$) interfaces were considered in the analyses.

Figure 12a shows the vertical penetration resistance from the SLA modelling, with both results remaining very nearly constant throughout the large imposed displacement. The average normalised resistances for smooth and rough pipes are 9.31 and 11.98 respectively, only slightly above the respective theoretical solutions. The bracketing discrepancy throughout each analysis is shown in Figure 12b, and is within 1.5% after the pipe has been displaced by $0.2D$.

Figure 13 presents failure mechanisms for different stages of the analysis. The pipe with the rough interface is found to develop a more extensive mechanism, but the surrounding soil experiences less

intense shearing. Small rigid wedges of soil above and below the pipe are found to move with the rough pipe, which is consistent with the theoretical solution of [3]. The results again indicate that the remeshing algorithm is performing satisfactorily.

3.4. Indentation of a smooth wedge

In this section, continuous indentation of a smooth wedge into weightless rigid–plastic Tresca material is studied. The analytical solution for this problem, derived by Hill et al. [69] using slip-line theory, is shown on the left of Figure 14. The initial surface of the indented material is OC, and the face of the wedge is AB. During continuous penetration of the wedge, the free surface at the edge of the plastic region remains straight, denoted by line AC. The region ABD moves as a rigid block parallel to BD, which is at 45° to the wedge face. ADE is a region of diffuse shear, with material moving on circular paths parallel to arc DE and centred at A. AEC moves as a rigid block parallel to EC, which is at 45° to AC. The relationship between the angles in Figure 14 is

$$\cos(\beta - \psi) = \frac{\cos \psi}{1 + \sin \psi} \quad (15)$$

Three wedges with apex angles, β , of 30° , 60° and 90° were pushed to a final depth, D , of 0.5 m. The dimensions $B/2$ and h of the SLA model (see Figure 9) were 2 m and 1.5 m respectively. The shear strength of the soil was taken as 1 kPa. The adopted values of δd and A_{min} were $0.01D$ and $0.001d^2$, the latter meaning that the mesh density varied during the indentation process as the penetration d increased. Adoption of a constant mesh density would have yielded less satisfactory results at very shallow indentation depths, where only a small region of soil is undergoing plastic deformation. A brief parametric study was performed to investigate the influence of δd and A_{min} on the solutions.

Figure 15 shows the SLA load–displacement responses for wedges with different apex angles, together with the theoretical solutions from [69]. There is excellent agreement between the numerical and analytical results. The right side of Figure 14 illustrates the adaptively refined mesh and the distribution of normalised shear strain rate $\dot{\gamma}D/v_p$ for the wedge with $\beta = 60^\circ$ at an indentation of 0.4 m. The SLA results show a rigid block adjacent to the wedge and another at

the surface, as well as a fan region of diffuse shear between the two rigid blocks, which is consistent with the mechanism in [69]. Most importantly, the free surface remains straight throughout the simulation, as predicted by the theoretical solution.

Figure 16a shows the influence of mesh density on the load–displacement response of a wedge with $\beta = 60^\circ$, showing that the UB solution for this problem is relatively insensitive to the mesh density. Figure 16b illustrates the bracketing discrepancy between the LB and UB solutions throughout the indentation. The discrepancy is found to decrease with mesh density, and can be limited to 2% by taking A_{min} below $0.005d^2$.

Figure 17a shows the influence of the displacement increment δd on the load–displacement response of a wedge with $\beta = 60^\circ$. For all the values of δd considered here, very good agreement between the SLA calculation and the theoretical solution is achieved. Figure 17b shows the overall volume change of the rigid–plastic material during the indentation, normalised as $\Delta Vol/D^2$, where ΔVol is the difference between the current and initial material volume in the entire model. For all of the analyses, $\Delta Vol/D^2$ is limited to 6×10^{-4} , demonstrating that numerically-induced volume change in the SLA procedure is extremely limited.

3.5. Indentation of a strip footing

For an infinitesimal vertical displacement, the classical strip footing bearing capacity problem has been solved analytically using slip-line theory [70]. The normalised capacity is given by $V_c/Ds_u = 2 + \pi$, where D is the footing width and s_u is the undrained shear strength. There is, however, no analytical solution for the case of further continuous indentation. Therefore for this example, the resistance, soil mechanism and surface configuration obtained from SLA modelling are compared with those obtained from CEL modelling using Abaqus.

The dimensions $B/2$ and h of the soil domain (see Figure 9) were $4D$ and $3D$ respectively. The strip footing was modelled as a rigid body comprised of four segments. The base was made fully rough ($\alpha = 1$) and the sides fully smooth ($\alpha = 0$). The soil was modelled as a weightless Tresca material with homogeneous shear strength, and the footing was pushed vertically to a depth of $0.5D$.

1 The values of A_{min} and δd were chosen to be $0.00025D^2$ and $0.001D$ following preliminary analyses
 2 studying the effect of these parameters on the results. In these preliminary analyses, the footing was
 3 penetrated to a final depth of $0.25D$ instead of $0.5D$. Note that in the CEL model, the shear strength
 4 of each interface was controlled by setting the maximum interface shear stress to be a fraction (equal
 5 to α as used in the SLA model) of the shear strength of the adjacent soil.

6 Figure 18a shows the influence of mesh density on the load–displacement response. Even
 7 the coarsest mesh, with $A_{min} = 0.00125D^2$, generates stable results with minimal fluctuations,
 8 demonstrating the stability of SLA in dealing with deep penetration problems. In all cases, the
 9 normalised bearing capacity calculated at the initial stage of loading, where the footing is just below
 10 the soil surface, is very close to the theoretical value of $2 + \pi$. The capacity increases approximately
 11 linearly with further indentation. Since the soil was modelled as weightless, it is clear that this
 12 increase in resistance is attributable to the enlargement of the plastically deforming soil region with
 13 depth, and the longer slip lines caused by soil heave. The bracketing discrepancy between the LB
 14 and UB results (Figure 18b) is limited to 1.5% in all cases, and only 0.8% for the finest mesh case,
 15 which was used for the main analyses described below.

16 Figure 19a shows the influence of the displacement increment δd on the load–displacement
 17 response. The result obtained from Abaqus CEL modelling [66] is provided for comparison. In
 18 the CEL model the footing was pushed to the desired depth of $0.5D$ at a quasi-static rate, to ensure
 19 that inertial effects were limited. As expected, the SLA loading curves agree very well with the
 20 theoretical solution at the start of loading, and then increase approximately linearly. Even with the
 21 largest incremental displacement ($\delta d/D = 0.005$) the results appear to be stable and reliable. In
 22 the initial stages of loading, the capacity obtained from the CEL analysis is lower than both the
 23 analytical value and the SLA curves. This is reasonable because in the CEL model, which uses
 24 elastic–plastic soil, the footing needs to be pushed further to develop a global failure mechanism.
 25 In the SLA model, which uses rigid–plastic soil, a global mechanism develops immediately (see
 26 Figures 20a and 20b). After the CEL curve reaches yield, indicating the development of a global
 27 failure mechanism, the capacity at a given penetration depth is higher than that obtained from

1 SLA. The observed stronger response for CEL is consistent with the failure mechanisms shown
 2 in Figure 20c, as the plastic region in the CEL analysis is found to be slightly larger than that
 3 in the SLA simulation. The reason why the CEL analysis develops a larger mechanism could
 4 possibly be attributed to the incorporation of elastic response, which cannot be captured in SLA.
 5 The discretisation error in the relatively coarse CEL mesh could also contribute to this difference.

6 Figure 19b shows the normalised change in material volume ($\Delta Vol/D^2$) during the SLA
 7 simulations. The volume change is found to increase with the number of incremental analyses in
 8 the sequence. This reveals that the remeshing involved in SLA modelling does inevitably introduce
 9 some degree of non-physical volume change. However, even for the case with the largest number
 10 of increments (and deepest embedment), the normalised volume change is limited to an extremely
 11 small value of 4.2×10^{-4} .

12 Figure 20 shows the soil failure mechanisms at different stages of the footing penetration. CEL
 13 results (left) are provided for comparison with the SLA results (right). Very good agreement is found
 14 throughout the loading process, except for the initial stage where a global failure mechanism is not
 15 yet fully developed in the CEL model (Figure 20a). A fan region, two rigid blocks and a perimeter
 16 slip line embracing the whole mechanism are visible, particularly in the SLA plots, revealing a
 17 classical Prandtl-like mechanism. Figure 20 confirms that throughout the loading process, highly
 18 refined meshes cover the areas of intense shearing in the SLA model.

19 3.6. Deep indentation of a pipe in rate-independent softening soil

20 Physical modelling of the deep penetration behaviour of a pipe segment in kaolin clay has been
 21 reported by Lee [71]. Small-scale model tests at unit gravity were completed, with the pipe
 22 penetrated vertically to a depth of more than $7D$. A mechanism transition from global to localised
 23 failure was observed during the penetration. Parameters related to the model test given by [71] are
 24 listed in Table II. For the SLA modelling, $B/2$ and h (see Figure 9) were both set to be $7D$, and the
 25 pipe was penetrated to an embedment of $4D$. The pipe displacement increment δd was chosen to be
 26 $0.005D$ and the minimum element size A_{min} was $0.00025D^2$.

Figure 21 shows the experimental load–penetration curve compared with the results from various simulations. The experimental curve is the average of several model tests, rather than data from a specific test; this averaged curve was the one used in [71] for comparisons with numerical modelling. SLA with non-softening soil moderately overestimates the penetration resistance by about 12%. SLA with softening soil can reasonably predict the loading response, especially at deep embedment, but underestimates the resistance at depths less than $2.5D$. A close match with the experimental curve over the whole depth of penetration cannot be achieved by the SLA simulations presented here. Also shown in Figure 21 is the bracketing discrepancy corresponding to the SLA simulation with softening soil. The discrepancy is within about 1.5% beyond an embedment of $0.5D$, which represents a high standard of computing accuracy considering that the material has a non-homogeneous initial strength profile and also undergoes significant strain softening. The normalised volume change of the material, $\Delta Vol/D^2$, is 2.4×10^{-3} at the end of the SLA simulation, indicating a very good approximation of constant-volume deformation.

Considering the uncertainty in quantifying the soil strength in small-scale model tests, in Figure 21 some alternative numerical results from Abaqus CEL modelling [66] are presented for comparison with the SLA data, and very good agreement between the two is observed. Whilst the SLA simulation was performed on a 4-core desktop computer with 4 GB RAM, the CEL analysis was completed on a 32-core cluster with 64 GB RAM. The SLA and CEL computing times for the softening soil case are 13661 s and 61520 s respectively, indicating a considerable advantage of SLA in computing efficiency. A fully objective comparison (same computer, similar mesh density, etc.) of computing times between SLA and CEL is very difficult to make, and this issue will be discussed further in Section 4.2.

Figure 22 provides comparisons of the soil failure mechanisms in the SLA and CEL simulations at different embedments. The deformation patterns of the two numerical analyses align very well, particularly given that different algorithms and element types were used. Since the model test was conducted at 1g at a very small scale, the effect of the soil weight was not as significant as it would be for a full-scale pipe in the field. As a result, backfilling of the soil over the pipe is absent in both

the physical modelling and the numerical simulations. Figure 23 shows the softening factor of the soil (the first bracketed term in Equation 10) at the end of loading, and there is good agreement between SLA and CEL. Note that the CEL analyses were performed with a user-defined material subroutine implementing Equation 10. In this subroutine the accumulated plastic shear strain, ξ , was updated using the difference between the major and minor principal strain increments. This is to be consistent with the definition used in the SLA formulation (see Section 2.2).

3.7. Shallow indentation of a pipe in rate-dependent softening soil

In this section, the SLA method is used to simulate a centrifuge model test reported by Dingle et al. [72], where a model pipe segment was penetrated vertically to a depth of $0.45D$. Key parameters from [72] are given in Table III. SLA modelling parameters concerning the effects of strain softening and strain rate were chosen according to the numerical studies reported in [73] and [49], as given in Table IV. An Abaqus CEL simulation was also conducted for comparison with the SLA simulation. For this validation study, $B/2$ and h (see Figure 9) were set as $5D$ and $4D$ respectively, whilst A_{min} was $0.00025D^2$ and δd was $0.002D$. The interface roughness factor α was set as 0.5 [73].

Figure 24 shows the experimental load–penetration curve compared with the results of the various numerical simulations. The resistance from the SLA prediction with ideal soil is significantly lower than the result of the model test. Even less resistance is predicted when the effect of strain softening is included. When the effects of both strain softening and strain rate are taken into account, a reasonable match with the model test can be achieved (see the curve corresponding to $\mu = 0.1$). The normalised bracketing discrepancy between the LB and UB results in the SLA simulation is shown for the case of $\mu = 0.1$. It is clear that satisfactory computing accuracy was achieved, with the discrepancy generally being kept within a range of 1 to 2%. The normalised volume change $\Delta Vol/D^2$ in this case (SLA with $\mu = 0.1$) was less than 1.3×10^{-3} at the end of loading. The CEL modelling results from [66] are also shown, and despite a greater degree of fluctuation, the trend of the CEL curves is found to compare well with the SLA results. The corresponding computing

1 times for these simulations were 780 s for SLA (4-core desktop, 4 GB RAM) and 7935 s for CEL
 2 (16-core cluster, 64 GB RAM).

3 Figure 25 shows a comparison of soil deformations between SLA and the centrifuge model test
 4 at the end of penetration ($d/D = 0.45$). There is very satisfactory agreement in both the shape and
 5 size of the deformed soil region. Since the softening factor of the soil (the first bracketed term in
 6 Equation 10) is not available for the centrifuge test, the results obtained from the CEL modelling are
 7 presented for comparison in Figure 26. In this example the SLA and CEL results differ considerably.
 8 Most noticeably, the displaced soil surface from the CEL analysis has a steeper slope compared with
 9 both the SLA simulation and the centrifuge model test. Also, the plastically deforming region is
 10 smaller in CEL than in SLA, and there is a more severe and localised softening effect. The moderate
 11 discrepancy between the two analyses could arise from their differing treatments of soil elasticity
 12 (present in CEL but absent in SLA). The elastic response must to some degree influence the soil
 13 failure mechanism, and subsequently the distribution of shear strength of the strain-softening soil.
 14 The resulting difference could accumulate and be exacerbated due to the complex deformations
 15 involved in this problem. It is hard to decide which analysis is closer to the physical reality, but
 16 comparison with the soil surface profile observed in the model test (see Figure 25) suggests that
 17 SLA exhibits more realistic behaviour in this instance. Another possible reason for the discrepancy
 18 is that the fixed-size CEL mesh is effectively very coarse during the early stages of pipe penetration,
 19 whereas the SLA modelling benefits from adaptive mesh refinement throughout the process.

20 3.8. Lateral loading behaviour of a pipe

21 A centrifuge model test investigating the monotonic lateral loading behaviour of a pipe segment
 22 was reported by Dingle et al. [72]. The pipe and soil parameters adopted for the SLA simulation of
 23 this test are as given in Table III and Table IV. The general arrangement and boundary conditions
 24 for the SLA model are illustrated in Figure 27. Fixed boundary conditions were applied to the two
 25 sides and the bottom of the soil domain, while the top was set as a free surface. The dimensions
 26 B_1 , B_2 and h were chosen to be $3D$, $7D$ and $3D$ whilst the minimum element size A_{min} was set as

0.00025 D^2 . The pipe displacement increment δd was set to 0.0025 D and 0.005 D for the vertical and lateral loading stages respectively. Tension was not allowed at the interface by default, but one case with unlimited tension was also modelled to study its effect on the initial break-out phase of the lateral loading stage. The interface roughness factor α was set as 0.5. The pipe was first pushed vertically into the soil to a depth of 0.45 D , after which it was displaced horizontally for a distance of 3 D under a constant vertical load of 3.3 kN/m (see Table III).

Figure 28 shows the centrifuge model test results as well as the numerical results, in terms of the pipe invert trajectory and the lateral load–displacement response. It is observed that when the effects of both strain rate and softening are considered in the SLA modelling, there is good agreement between the experimental and numerical results. The computing time for this SLA simulation was 11094 s. The analysis with ideal soil (rate-independent, no softening) largely overestimates the lateral resistance. The analysis with rate-independent softening soil moderately underestimates the resistance at the start of the lateral loading phase, but yields the most satisfactory results near the end. During the initial lateral break-out, a sharp increase in resistance is observed in the centrifuge model test results (Figure 28b). This can be attributed to tensile stresses mobilised at the rear of the pipe, sustained by transient pore water suctions. This behaviour is absent in the numerical results where tensile normal stress was not permitted at the pipe–soil interface. Figure 28b also shows the results of an SLA simulation of the initial lateral break-out phase with unlimited tension allowed at the interface. Here the experimental break-out resistance is moderately overestimated. The peak resistance measured in the centrifuge test is found to be between the two extremes of no tension and full tension at the interface. Though not shown in Figure 28, the largest normalised volume change, $\Delta Vol/D^2$, at the end of lateral loading for all of the SLA simulations was about 5×10^{-3} .

Figure 29 shows the soil failure mechanisms at various points during the SLA simulation of the lateral loading stage, with observations from the centrifuge model test [72] also presented (inset) for comparison. It can be seen that the soil deformations obtained from SLA agree very well with those from the model test throughout the lateral loading process. Moderate differences can be found at the end of loading, where SLA produces a steeper slope in the active berm. This could be attributed

1 to the fact that the soil strength at very shallow depth is likely to be overestimated in the SLA
 2 simulation, as a result of using a linear fit to approximate the experimentally measured strength
 3 profile. This means that when the surficial soil is scraped by the pipe to form the active berm, the
 4 berm will be stronger in the SLA simulation than in the centrifuge test.

5 Figures 30a and 30b show the strength reduction factor due to softening (the first bracketed term
 6 in Equation 10) at different stages of lateral loading. It can be seen that the soil within the active
 7 berm has become severely softened by the end of loading. Of most importance is that, with six-
 8 noded triangular elements being used to perform quadratic interpolation of field variables when
 9 the model is remeshed, there is no significant numerically-induced ‘pollution’ of the field variables.
 10 This can be checked by comparison of the softening factor distribution in the left-hand berm, behind
 11 the pipe, between Figures 30a and 30b.

12 Figure 30c shows the strength enhancement factor due to strain rate (the second bracketed term
 13 in Equation 10) at the end of loading. The area influenced by the strain rate effect is very localised,
 14 though the soil strength within the deforming region is enhanced by about 50%. Figure 30d shows
 15 the combined strength modification factor of the soil, with both strain softening and strain rate
 16 effects being taken into account. It can be observed in Figures 30b and 30c that the regions being
 17 softened and those being enhanced hardly coincide. Therefore the combined strength modification
 18 factor in Figure 30d varies over a very wide range, suggesting that in complex problems such as
 19 this, the influences of strain softening and strain rate do not counterbalance, and must be accounted
 20 for as separate effects.

4. DISCUSSION

21 4.1. Treatment of numerical difficulties

22 Minor numerical fluctuations in an SLA solution are inevitable because the model configuration is
 23 updated using a finite time step Δt , regular remeshing is performed, and small errors are introduced
 24 by the interpolation of field variables. However, more serious difficulties can arise occasionally.

For instance, in modelling the lateral movement of a rigid body under a constant vertical load (as described in Section 3.8), the vertical load may be close to the vertical bearing capacity. In moving from one increment to the next, the new vertical bearing capacity may be lower than the vertical load, so that the model collapses without the opportunity for further lateral loading. Such a situation can be detected when the nodal velocities obtained from the UB analysis are unrealistically large (e.g. over 10^6 times the rigid body velocity). Similarly, there may be slope instability issues encountered as a result of an ill-shaped gap or a steep slope (Figure 31), which need to be resolved in order for the analysis sequence to continue. These difficulties are particularly relevant to the large-displacement problems explored in Sections 3.6 and 3.8.

The approach used in the present SLA simulations is that once a collapse situation is detected, the rigid body is temporarily forced to move under pure displacement control, if applicable. For example, in the lateral loading of a pipe under constant vertical load, the downward velocity can be temporarily set as some fraction (e.g. 20%) of the lateral velocity. If the instability cannot be resolved in this way, the controlling code then checks to see if there are stability problems caused by an ill-shaped gap or a steep slope.

To deal with an ill-shaped gap (Figure 31a), a critical surface node must be found. The criterion to determine such a node $n_{(p)}$ is that its horizontal coordinate should be closer to the rigid body centre than two adjacent nodes, $n_{(p-1)}$ and $n_{(p+1)}$. The vertical coordinate of such a node should also be lower than the centre of the rigid body, otherwise, a node such as $n_{(q)}$ in Figure 31a will be mistakenly recognised to form a 'gap'. Node $n_{(p)}$ is then removed from the list of free surface nodes. A new model is then generated based on the reconstructed surface. This process is repeated until the slope instability issue has been resolved or a critical surface node cannot be found.

To handle collapse of a steep slope above the crown of a deeply penetrated rigid body (Figure 31b), an auxiliary domain slightly larger than the rigid body but of exactly the same shape is established. All surface nodes are checked to see if they can be located within this domain. If such a node is found (see $n_{(p-2)}$, $n_{(p-1)}$ and $n_{(p)}$ in Figure 31b), it is projected perpendicularly onto the nearest rigid body segment in an attempt to restore the slope stability. Of all the nodes that meet the

1 criterion, the one with the largest index number (here $n_{(p)}$) is recognised as the new margin node
 2 (Figure 2). The surface is then reconstructed and a new model is generated for a fresh attempt at the
 3 current increment. An iterative approach is adopted, with the auxiliary domain starting from a size
 4 of $1.005D$ and increasing at an interval of $0.005D$, finishing when the collapse situation has been
 5 resolved or the auxiliary domain has reached a size of $1.05D$. In some extreme cases such as deep
 6 penetration of a rigid body into highly softening soil (e.g. $S_t \geq 20$, $\xi_{95} = 10$), a satisfactory solution
 7 cannot be found and the analysis must be terminated.

8 The problem resolution strategies described here are clearly not theoretically robust or general,
 9 but they have proved to be very effective *ad hoc* solutions for the problems studied in this paper
 10 and others considered in [66]. For other problems new strategies may be necessary. For example,
 11 in an analysis involving very deep embedment of a rigid body, free surfaces from two directions
 12 may come into contact, with the nodes of the two surfaces penetrating into each other (or the nodes
 13 of a free surface penetrating into the symmetry boundary when only half the model is analysed).
 14 Since these situations are limited to very specific cases, the strategies used to handle them are not
 15 introduced here, but can be found in [66].

16 4.2. Computation times

17 The computing times required for the present SLA implementation to perform the different
 18 benchmark analyses are summarised in Table V. Only the time for the default case of each problem
 19 is provided. The computing efficiency of SLA is considered to be very attractive, as even the two
 20 cases with total displacements of more than three pipe diameters, and where severe variations of
 21 material strength are involved, take less than four hours to complete on a desktop computer.

22 It is difficult to make a general assessment of the computing efficiency of SLA for large-
 23 deformation problems, as the number of elements in the model varies considerably during an
 24 individual analysis, due to the employment of the adaptive remeshing strategy described in Section
 25 2.3. This issue also makes it very hard to achieve an objective comparison of computing efficiency
 26 between SLA (drastically varying number of elements) and CEL analysis (constant number of

elements). Moreover, whilst the SLA analyses were performed on a desktop computer with 4 cores and 4 GB RAM, most of the CEL analyses could only be carried out on a cluster with 16 to 32 cores and 64 GB RAM. The different element types (2D second-order triangle for SLA and 3D first-order brick for CEL) also contribute to the difficulty of making such a comparison. However, the focus of Table V is to demonstrate that numerical modelling using SLA is very efficient in absolute terms, rather than more efficient by comparison with other particular methods such as CEL analysis.

One reason for the efficiency of SLA lies in the fact that it avoids the need to keep track of stresses at integration points, for use in elastic-plastic constitutive equations [24]. As a consequence, SLA can generate reliable results using relatively coarse meshes for each individual FELA solution in the sequence, and for the interpolation of field variables. More importantly, as tested in the benchmark studies, reliable geometric updating can be achieved in SLA even when using large incremental displacements ($0.002D$ to $0.005D$). These are significantly greater than the incremental displacements used in the complementary CEL analyses (automatically chosen by Abaqus but typically of order $10^{-5}D$). This means that the same problem can be completed with fewer increments in SLA than in CEL or in other FE methods.

5. CONCLUSIONS

This paper has described the development of a sequential limit analysis (SLA) method for solving large-deformation plane strain plasticity problems involving rigid bodies interacting with purely cohesive (undrained) soils. The treatments of interfaces, boundaries and material properties during large plastic deformations have been described in detail. A widely used total stress constitutive model [61] was adopted to take into account the strain-softening and rate-dependent behaviour of the soil strength.

Mesh distortion was avoided by regular remeshing of the model. The meshing strategy developed for the SLA simulations proved to be highly reliable, with areas experiencing severe remoulding or intense shear strain rates being targeted with higher mesh densities. In the SLA method no mapping

1 of stresses is needed during the interpolation stage, which is beneficial for numerical stability and
 2 computing efficiency.

3 The treatment of evolving interfaces and boundaries in SLA modelling inevitably introduces some
 4 spurious volume change for the (assumed) incompressible rigid-plastic material. However, for all of
 5 the problems investigated in this paper, the cumulative volume change was found to be very limited
 6 by comparison with the volume of the rigid body driving the process (ratio of order 10^{-3} or less),
 7 and therefore unlikely to influence the overall model response.

8 A detailed verification and validation study has been presented, using both analytical plasticity
 9 solutions and physical model test results. Excellent agreement was found between SLA simulation
 10 results and theoretical solutions from slip-line theory, indicating that the approach is robust. When
 11 taking into account the effects of strain softening and strain rate on the undrained shear strength
 12 of the soil, the SLA approach was able to generate very satisfactory predictions of both 1g
 13 and centrifuge model tests on pipeline segments causing large plastic deformations of soft clay
 14 specimens.

15 Possible areas for future work include extension of the present SLA approach to axially symmetric
 16 and three-dimensional problems, and to situations where collapse of the soil is driven by gravity
 17 rather than by a rigid body. The use of mesh-free methods to obtain (non-strict) upper bound limit
 18 analysis solutions (e.g. [74, 75]) could also be worth exploring in the context of SLA.

19 REFERENCES

- 20
- 21 1. Gvozdev AA. The determination of the value of the collapse load for statically indeterminate systems undergoing
 22 plastic deformation. *International Journal of Mechanical Sciences* 1960; **1**(4):322–335.
 - 23 2. Drucker DC, Prager W, Greenberg HJ. Extended limit design theorems for continuous media. *Quarterly of Applied*
 24 *Mathematics* 1952; **9**:381–389.
 - 25 3. Randolph MF, Houlsby GT. The limiting pressure on a circular pile loaded laterally in cohesive soil. *Géotechnique*
 26 1984; **34**(4):613–623.
 - 27 4. Martin CM, Randolph MF. Upper bound analysis of lateral pile capacity in cohesive soil. *Géotechnique* 2006;
 28 **56**(2):141–145.

- 1 5. Randolph MF, Martin CM, Hu Y. Limiting resistance of a spherical penetrometer in cohesive material.
2 *Géotechnique* 2000; **50**(5):573–582.
- 3 6. Martin CM. Vertical bearing capacity of skirted circular foundations on Tresca soil. *Proc. 15th Int. Conf. on Soil*
4 *Mechanics and Geotechnical Engineering*, Istanbul, 2001; 743–746.
- 5 7. Lysmer J. Limit analysis of plane problems in soil mechanics. *Journal of the Soil Mechanics and Foundations*
6 *Division (ASCE)* 1970; **96**:1311–1334.
- 7 8. Anderheggen E, Knöpfel H. Finite element limit analysis using linear programming. *International Journal of Solids*
8 *and Structures* 1972; **8**:1413–1431.
- 9 9. Pastor J. Analyse limite: détermination numérique de solutions statiques complètes. application au talus vertical.
10 *Journal de Mécanique Appliquée* 1978; **2**:167–196.
- 11 10. Sloan SW. Lower bound limit analysis using finite elements and linear programming. *International Journal for*
12 *Numerical and Analytical Methods in Geomechanics* 1988; **12**(1):61–77.
- 13 11. Sloan SW, Kleeman PW. Upper bound limit analysis using discontinuous velocity fields. *Computer Methods in*
14 *Applied Mechanics and Engineering* 1995; **127**(1–4):293–314.
- 15 12. Gao Y. Panpenalty finite element programming for plastic limit analysis. *Computers and Structures* 1988; **28**:749–
16 755.
- 17 13. Zouain N, Herskovits J, Borges L, Feijóo R. An iterative algorithm for limit analysis with nonlinear yield functions.
18 *International Journal of Solids and Structures* 1993; **30**:1397–1417.
- 19 14. Borges L, Zouain N, Huespe A. A nonlinear optimization procedure for limit analysis. *European Journal of*
20 *Mechanics A/Solids* 1996; **15**:487–512.
- 21 15. Andersen KD, Christiansen E, Overton ML. Computing limit loads by minimizing a sum of norms. *SIAM Journal*
22 *on Scientific Computing* 1998; **19**(3):1046–1062.
- 23 16. Lyamin AV, Sloan SW. Lower bound limit analysis using non-linear programming. *International Journal for*
24 *Numerical Methods in Engineering* 2002; **55**:573–611.
- 25 17. Lyamin AV, Sloan SW. Upper bound limit analysis using linear finite elements and non-linear programming.
26 *International Journal for Numerical and Analytical Methods in Geomechanics* 2002; **26**:181–216.
- 27 18. Makrodimopoulos A, Martin CM. Lower bound limit analysis of cohesive-frictional materials using second-order
28 cone programming. *International Journal for Numerical Methods in Engineering* 2006; **66**(4):604–634.
- 29 19. Makrodimopoulos A, Martin CM. Upper bound limit analysis using simplex strain elements and second-order cone
30 programming. *International Journal for Numerical and Analytical Methods in Geomechanics* 2007; **31**:835–865.
- 31 20. Krabbenhoft K, Lyamin AV, Sloan SW. Formulation and solution of some plasticity problems as conic programs.
32 *International Journal of Solids and Structures* 2007; **44**(5):1533–1549.
- 33 21. Makrodimopoulos A, Martin CM. Upper bound limit analysis using discontinuous quadratic displacement fields.
34 *Communications in Numerical Methods in Engineering* 2008; **24**:911–927.
- 35 22. Martin CM, Makrodimopoulos A. Finite-element limit analysis of Mohr-Coulomb materials in 3D using
36 semidefinite programming. *Journal of Engineering Mechanics* 2008; **134**(4):339–347.

- 1 23. Pastor F, Loute E, Pastor J, Trillat M. Mixed method and convex optimization for limit analysis of homogeneous
2 Gurson materials: a kinematical approach. *European Journal of Mechanics A/Solids* 2009; **28**(1):25–35.
- 3 24. Yang WH. Large deformation of structures by sequential limit analysis. *International Journal of Solids and*
4 *Structures* 1993; **30**(7):1001–1013.
- 5 25. Hwan CL. An upper bound finite element procedure for solving large plane strain deformation. *International*
6 *Journal for Numerical Methods in Engineering* 1997; **40**:1909–1922.
- 7 26. Raithatha A, Duncan SR. Rigid plastic model of incremental sheet deformation using second-order cone
8 programming. *International Journal for Numerical Methods in Engineering* 2008; **78**:955–979.
- 9 27. Martin CM. The use of adaptive finite-element limit analysis to reveal slip-line fields. *Géotechnique Letters* 2011;
10 **1**:23–29.
- 11 28. Shewchuk JR. Delaunay refinement algorithms for triangular mesh generation. *Computational Geometry* 2002;
12 **47**:741–778.
- 13 29. Ayachit U. *The ParaView Guide: A Parallel Visualization Application*. Kitware Inc., 2015.
- 14 30. MOSEK ApS. *The MOSEK optimization tools manual, Version 7*. 2013.
- 15 31. Burgess D, Sulsky D, Brackbill JU. Mass matrix formulation of the FLIP particle-in-cell method. *Journal of*
16 *Computational Physics* 1992; **103**:1–15.
- 17 32. Sulsky D, Chen Z, Schreyer HL. A particle method for history-dependent materials. *Computer Methods in Applied*
18 *Mechanics and Engineering* 1994; **118**:179–196.
- 19 33. Zhou SJ. The numerical prediction of material failure based on the material point method. PhD Thesis, University
20 of New Mexico 1998.
- 21 34. Coetzee CJ, Vermeer PA, Basson AH. The modelling of anchors using the material point method. *International*
22 *Journal for Numerical and Analytical Methods in Geomechanics* 2005; **29**:879–895.
- 23 35. Gingold RA, Monaghan JJ. Smoothed particle hydrodynamics: theory and application to non-spherical stars.
24 *Monthly Notices of the Royal Astronomical Society* 1977; **181**:375–389.
- 25 36. Monaghan JJ. Smoothed particle hydrodynamics. *Annual Review of Astronomy and Astrophysics* 1992; **30**:543–574.
- 26 37. Benz W, Asphaug E. Simulations of brittle solids using smoothed particle hydrodynamics. *Computer Physics*
27 *Communications* 1995; **87**(1-2):253–265.
- 28 38. Bonet J, Lok TSL. Variational and momentum preservation aspects of smooth particle hydrodynamic formulations.
29 *Computer Methods in Applied Mechanics and Engineering* 1999; **180**(1-2):97–115.
- 30 39. Cundall PA. A computer model for simulating progressive, large-scale movements in blocky rock systems.
31 *International Symposium on Rock Fracture*, Nancy, France, 1971; Paper No. II–8.
- 32 40. Cundall PA, Strack ODL. A discrete numerical model for granular assemblies. *Géotechnique* 1979; **29**(1):47–65.
- 33 41. O’Sullivan C. The application of discrete element modelling to finite deformation problems in geomechanics. PhD
34 Thesis, University of California 2002.
- 35 42. Zhou H, Randolph MF. Computational techniques and shear band development for cylindrical and spherical
36 penetrometers in strain-softening clay. *International Journal of Geomechanics* 2007; **7**(4):287–295.

- 1 43. Zdravkovic L, Carter J. Contributions to Géotechnique 1948-2008: Constitutive and numerical modelling.
2 *Géotechnique* 2008; **58**(5):405–412.
- 3 44. Macaro G. Distinct element modelling of pipe-soil interaction for offshore pipelines on granular soils. DPhil thesis,
4 University of Oxford 2015.
- 5 45. Hesar M. Pipeline-seabed interaction in soft clay. *Proc. 23rd Int. Conf. on Offshore Mechanics and Arctic*
6 *Engineering*, Vancouver, 2004; Paper No. OMAE2004–51 425.
- 7 46. Konuk I, Yu S. Continuum FE modelling of lateral buckling: study of soil effects. *Proc. 26th Int. Conf. on Offshore*
8 *Mechanics and Arctic Engineering*, San Diego, 2007; Paper No. OMAE2007–29 376.
- 9 47. Hu Y, Randolph MF. A practical numerical approach for large deformation problems in soil. *International Journal*
10 *for Numerical and Analytical Methods in Geomechanics* 1998; **22**:327–350.
- 11 48. Wang D, White DJ, Randolph MF. Large-deformation finite element analysis of pipe penetration and large-
12 amplitude lateral displacement. *Canadian Geotechnical Journal* 2009; **47**:842–856.
- 13 49. Chatterjee S, Randolph MF, White DJ. The effects of penetration rate and strain softening on the vertical penetration
14 resistance of seabed pipelines. *Géotechnique* 2012; **62**(7):573–582.
- 15 50. Chatterjee S, White DJ, Randolph MF. Numerical simulations of pipe-soil interaction during large lateral
16 movements on clay. *Géotechnique* 2012; **62**(8):693–705.
- 17 51. Abadalla B, Pike K, Eltaher A, Jukes P, Duron B. Development and validation of a coupled Eulerian Lagrangian
18 finite element ice scour model. *Proc. 28th Int. Conf. on Ocean, Offshore and Arctic Engineering*, Honolulu, 2009;
19 Paper No. OMAE2009–79 553.
- 20 52. Qiu G, Grabe J. Explicit modeling of cone and strip footing penetration under drained and undrained conditions
21 using a visco-hypoplastic model. *Geotechnik* 2011; **34**:205–217.
- 22 53. Zheng J, Hossain M, Wang D. 3D large deformation FE analysis of spudcan foundation on layered clays using CEL
23 approach. *2nd Int. Symp. on Constitutive Modeling of Geomaterials*, International Society of Offshore and Polar
24 Engineers: Anchorage, Alaska, 2012; 803–810.
- 25 54. Tho KK, Leung CF, Chow YK, Somsak S. Eulerian finite element simulation of spudcan–pile interaction. *Canadian*
26 *Geotechnical Journal* 2013; **50**(6):595–608.
- 27 55. Andresen L, Khoa HDV. *LDFE analysis of installation effects for offshore anchors and foundations*. Installation
28 Effects in Geotechnical Engineering, Taylor & Francis Group: London, 2013.
- 29 56. Martin CM, Kong D, Byrne BW. 3D analysis of transverse pipe–soil interaction using 2D soil slices. *Géotechnique*
30 *Letters* 2013; **3**(3):119–123.
- 31 57. Hawlader B, Dutta S, Fouzder A, Zakeri A. Penetration of steel catenary riser in soft clay seabed: Finite-element
32 and finite-volume methods. *International Journal of Geomechanics* 2015; **15**(6).
- 33 58. Dutta S, Hawlader B, Phillips R. Finite element modeling of partially embedded pipelines in clay seabed using
34 Coupled Eulerian–Lagrangian method. *Canadian Geotechnical Journal* 2015; **52**:58–72.
- 35 59. Klar A, Osman AS, Bolton M. 2D and 3D upper bound solutions for tunnel excavation using ‘elastic’ flow fields.
36 *International Journal for Numerical and Analytical Methods in Geomechanics* 2007; **31**(12):1367–1374.

- 1 60. Mollon G, Dias D, Soubra AH. Continuous velocity fields for collapse and blowout of a pressurized tunnel face
2 in purely cohesive soil. *International Journal for Numerical and Analytical Methods in Geomechanics* 2013;
3 **37**(13):2061–2083.
- 4 61. Einav I, Randolph MF. Combining upper bound and strain path methods for evaluating penetration resistance.
5 *International Journal for Numerical Methods in Engineering* 2005; **63**(14):1991–2016.
- 6 62. Randolph MF. Characterization of soft sediments for offshore applications. *Proc. 2nd Int. Conf. on Site*
7 *Characterization*, Porto, Portugal, 2004; 209–231.
- 8 63. Biscontin G, Pestana JM. Influence of peripheral velocity on vane shear strength of an artificial clay. *Geotechnical*
9 *Testing Journal* 2001; **24**(4):423–429.
- 10 64. Lunne T, Andersen KH. Soft clay shear strength parameters for deepwater geotechnical design. *Proc. 6th Int.*
11 *Offshore Site Investigation and Geotechnics Conf.*, vol. 1, London, 2007; 151–176.
- 12 65. TECPLOT. *Version 5 users manual*. Amtec Engineering, 1992.
- 13 66. Kong D. Large displacement numerical analysis of offshore pipe-soil interaction on clay. DPhil thesis, University
14 of Oxford 2015.
- 15 67. Dassault Systèmes. *Abaqus analysis users manual (6.11)*. Simula Corp, Providence, RI, USA, 2011.
- 16 68. Rowe RK, Davis EH. The behaviour of anchor plates in clay. *Géotechnique* 1982; **32**(1):9–23.
- 17 69. Hill R, Lee EH, Tupper SJ. The theory of wedge indentation of ductile materials. *Proceedings of the Royal Society*
18 *A* 1947; **188**:273–289.
- 19 70. Prandtl L. Über die Eindringungsfestigkeit Plastischer Baustoffe und die Festigkeit von Schneiden. *Z. Angew. Math.*
20 *Mech* 1921; **1**:15–20.
- 21 71. Lee YS. Physical and numerical modelling of pipe-soil interaction in clay. PhD Thesis, University of Sheffield
22 2012.
- 23 72. Dingle HRC, White DJ, Gaudin C. Mechanisms of pipe embedment and lateral breakout on soft clay. *Canadian*
24 *Geotechnical Journal* 2008; **45**:636–652.
- 25 73. Wang D, Hu Y, Randolph MF. Three-dimensional large deformation finite-element analysis of plate anchors in
26 uniform clay. *Journal of Geotechnical and Geoenvironmental Engineering* 2010; **136**(2):355–365.
- 27 74. Liu F, Zhao J. Upper bound limit analysis using radial point interpolation meshless method and nonlinear
28 programming. *International Journal of Mechanical Sciences* 2013; **70**:26–38.
- 29 75. Binesh SM, Raei S. Upper bound limit analysis of cohesive soils using mesh-free method. *Geomechanics and*
30 *Geoengineering* 2014; **9**(4):265–278.

Table I. Summary of numerical examples

Problem	Compared with	Free surface	Strain softening	Strain rate
Buried plate	Analytical [68]	–	–	–
Buried pipe	Analytical [3, 4]	–	–	–
Wedge	Analytical [69]	✓	–	–
Strip footing	Analytical [70]; CEL [66]	✓	–	–
Pipe (deep penetration)	1g model test [71]; CEL [66]	✓	✓	–
Pipe (shallow penetration)	Centrifuge test [72]; CEL [66]	✓	✓	✓
Pipe (lateral loading)	Centrifuge test [72]	✓	✓	✓

Table II. 1g model test parameters from [71]

Parameter	Value
Pipe diameter, D : m	0.03
Shear strength of soil at mudline, s_{um} : kPa	1.1
Shear strength gradient, ρ : kPa/m	4.5
Submerged unit weight of soil, γ' : kN/m ³	6
Final pipe embedment, w_{fin}	$7D$
Vertical penetration rate, v_p	$0.1D/s$
Pipe–soil interface roughness factor, α	0
Sensitivity of soil, S_t	1.7
Ductility parameter of soil, ξ_{95}	10

Table III. Centrifuge model test parameters (prototype scale) from [72]

Parameter	Value
Pipe diameter, D : m	0.8
Shear strength of soil at mudline, s_{um} : kPa	2.3
Shear strength gradient, ρ : kPa/m	3.6
Submerged unit weight of soil, γ' : kN/m ³	6.5
Initial pipe embedment, w_{ini}	$0.45D$
Final lateral displacement, u_{fin}	$3D$
Pipe weight during lateral displacement, W : kN/m	3.3
Vertical penetration rate, v_p	$0.015D/s$
Lateral displacement rate, v_p	$0.050D/s$

Table IV. Soil modelling parameters from [73] and [49]

Parameter	Value
Rate of strength increase per decade, μ	0.1
Reference shear strain rate, $\dot{\gamma}_{ref}$: s ⁻¹	3×10^{-6}
Sensitivity, S_t	3.2
Ductility parameter, ξ_{95}	10

Table V. Computational times of SLA simulations

Problem	Total displacement	Time: s
Buried plate	$1D$	3248
Buried pipe	$1D$	849
Wedge	0.5 m	1399
Strip footing	$0.5D$	1970
Pipe (deep penetration)	$4D$	13661
Pipe (shallow penetration)	$0.45D$	780
Pipe (lateral loading)	$3.45D$	11094

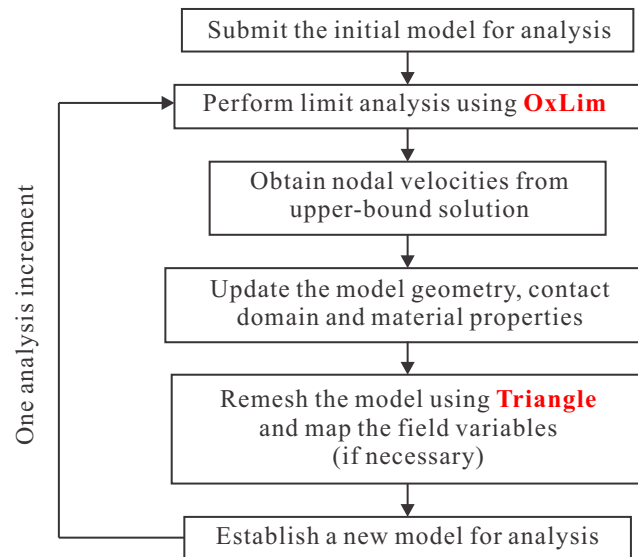


Figure 1. Overall scheme of the SLA approach.

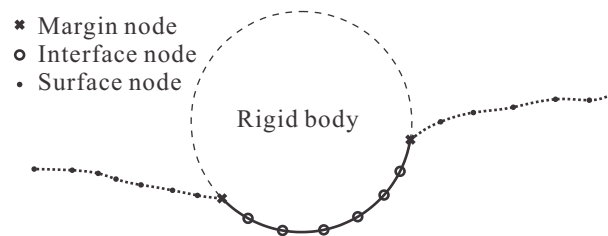


Figure 2. External boundary nodes.

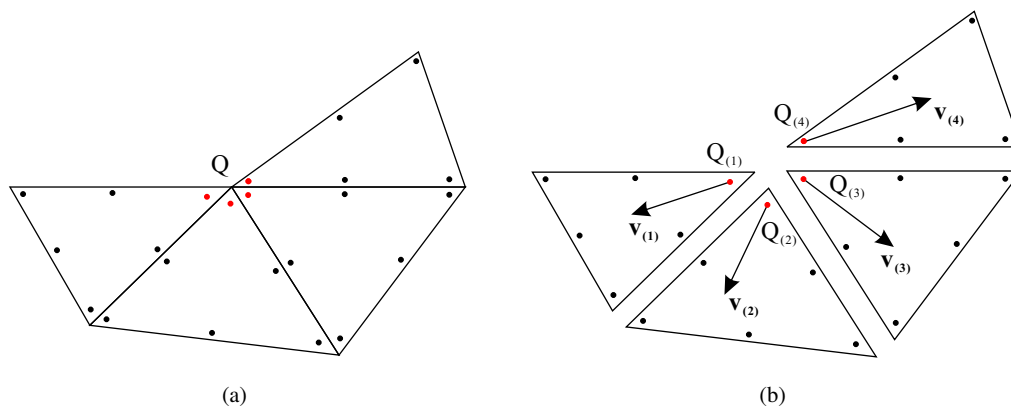


Figure 3. Nodal velocities in OxLim UB analysis: (a) evaluation points associated with node Q; (b) different velocity vectors of evaluation points (with exaggerated discrepancy).

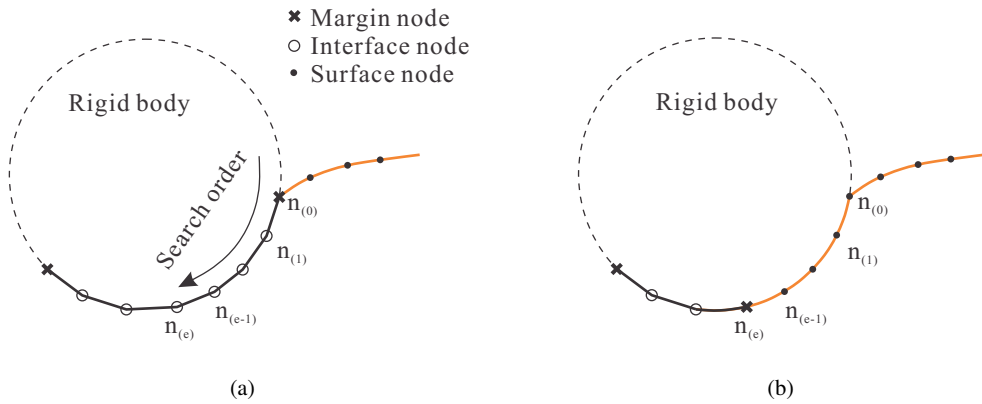


Figure 4. Interface nodes breaking away from a rigid body: (a) before break; (b) after break. Only the breakaway of the right margin node is shown.

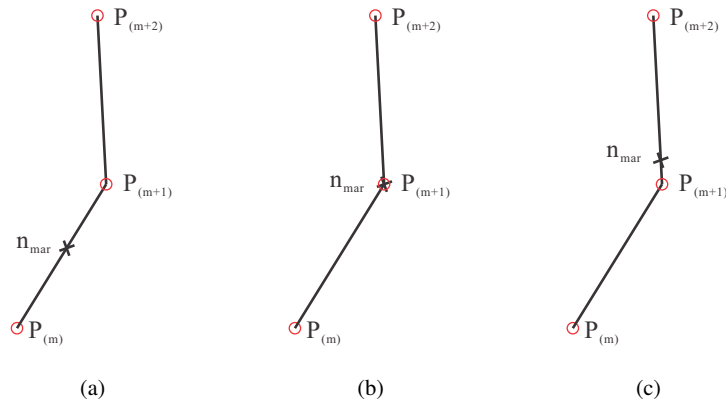


Figure 5. Schematic of 'jump' of a margin node: (a) before coordinate update; (b) time increment chosen to produce overlap after coordinate update; (c) margin node forced to 'jump' onto next rigid body segment.

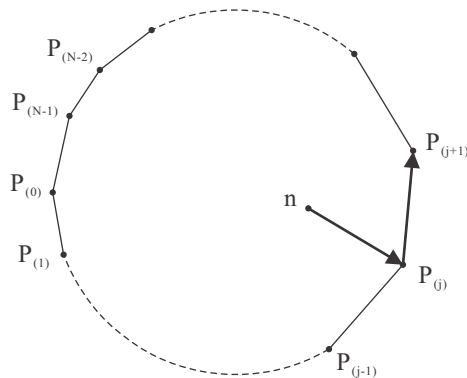


Figure 6. Determining if a point is inside a convex domain.

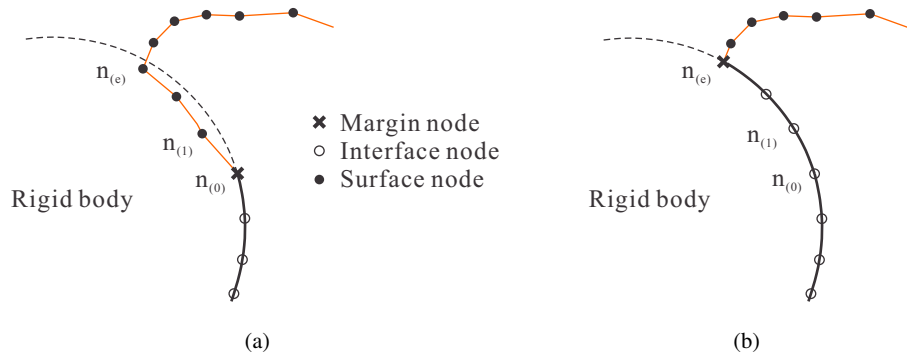


Figure 7. Handling of nodes that penetrate into a rigid body: (a) before treatment; (b) after treatment.

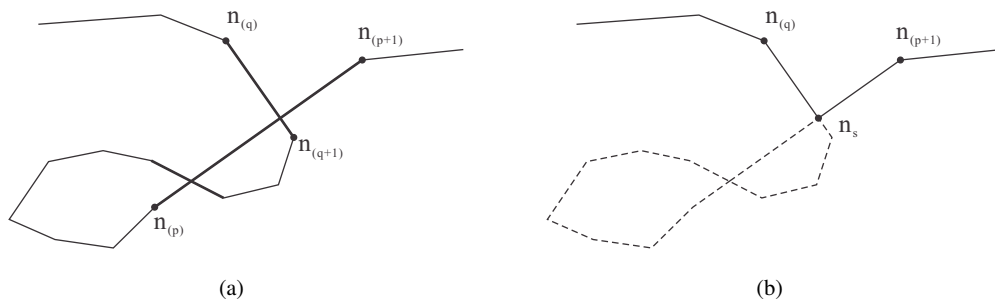


Figure 8. Handling self-contact of a free surface: (a) nodes encroaching into the surface; (b) reconstruction of the surface.

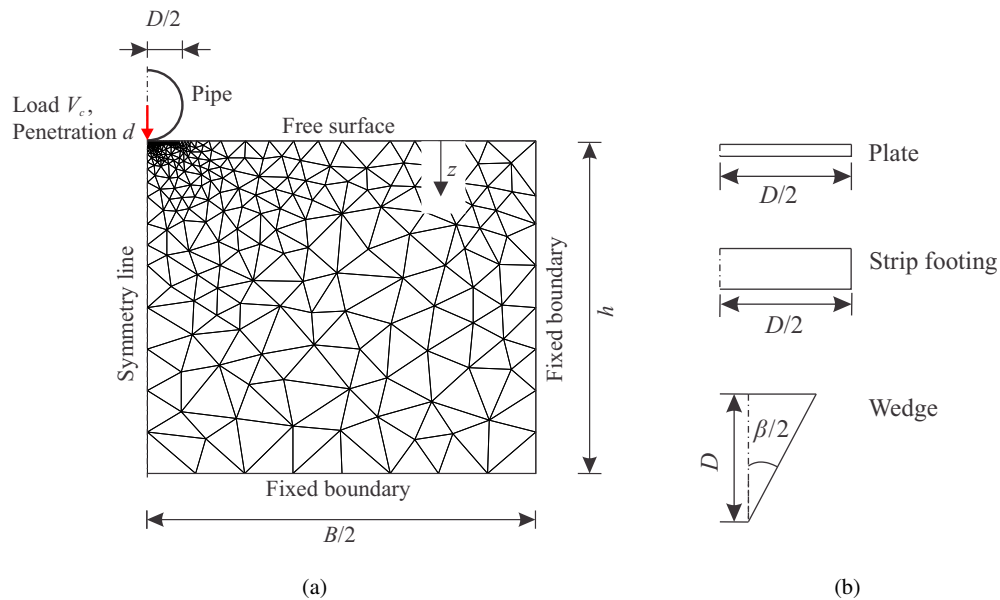


Figure 9. Initial configuration of SLA model for continuous indentation of a rigid body: (a) penetration of a pipe; (b) other rigid bodies.

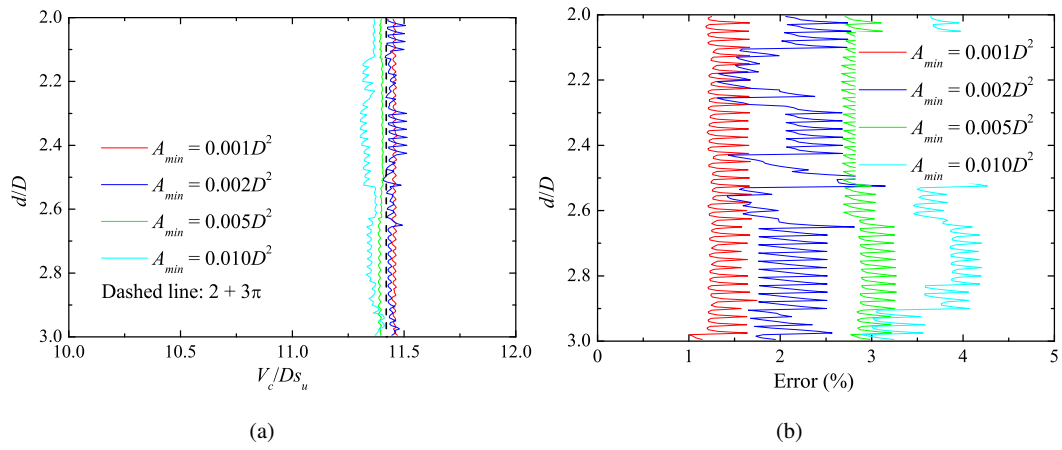


Figure 10. Vertical loading response of buried plate: (a) normalised resistance; (b) normalised bracketing discrepancy.

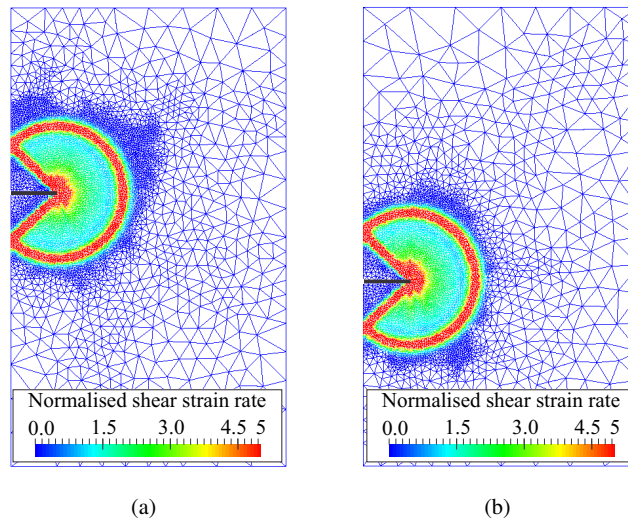


Figure 11. Soil failure mechanisms (contours of $\dot{\gamma}D/v_p$) for buried plate: (a) initial, $d/D = 2$; (b) final, $d/D = 3$.

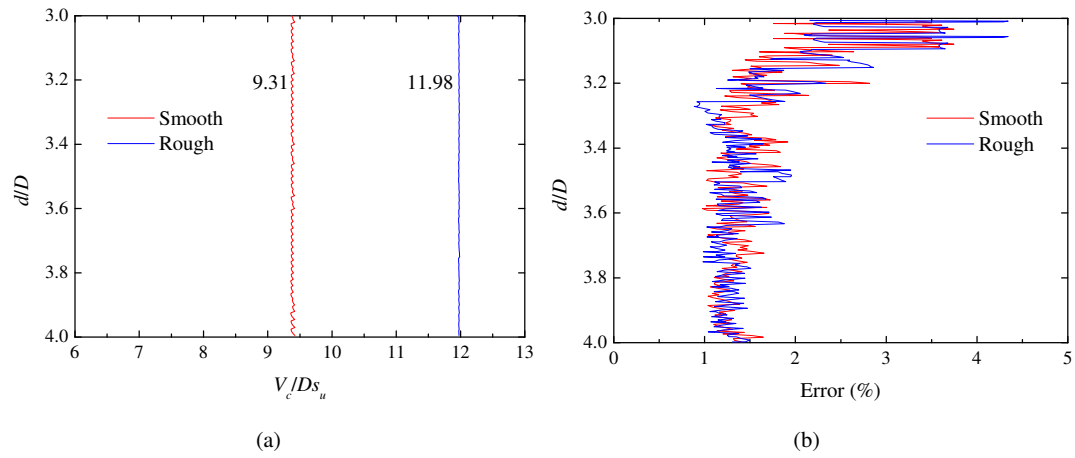


Figure 12. Vertical loading response of buried pipe: (a) normalised resistance; (b) normalised bracketing discrepancy.

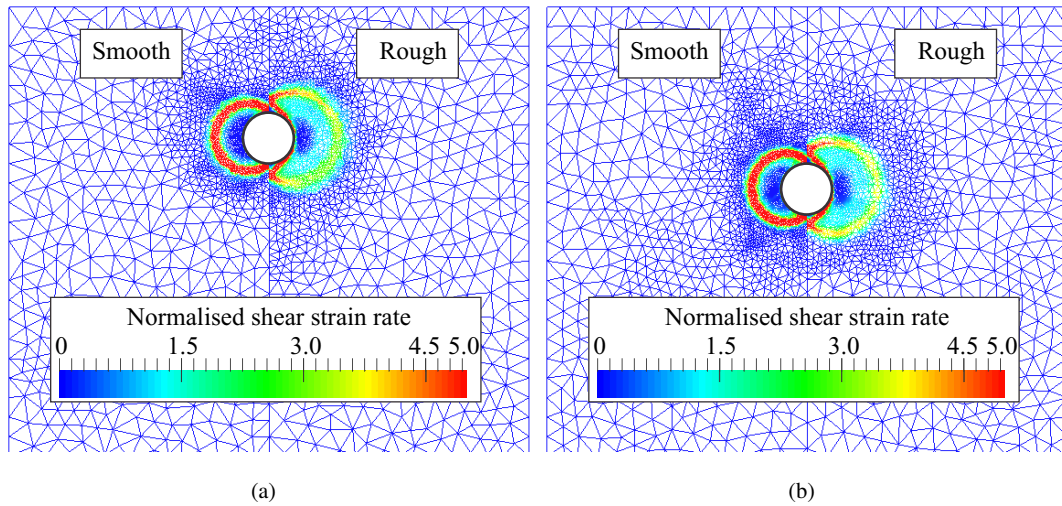


Figure 13. Soil failure mechanisms (contours of $\dot{\gamma}D/v_p$) for buried pipe: (a) initial, $d/D = 3$; (b) final, $d/D = 4$.

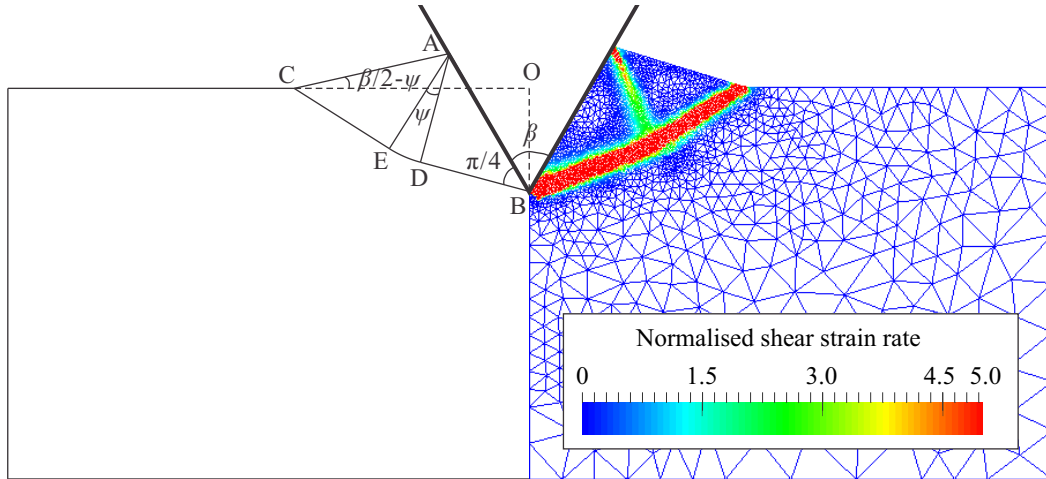


Figure 14. Soil failure mechanisms (contours of $\dot{\gamma}D/v_p$) for wedge. $\beta = 60^\circ$, $d = 0.4$ m.

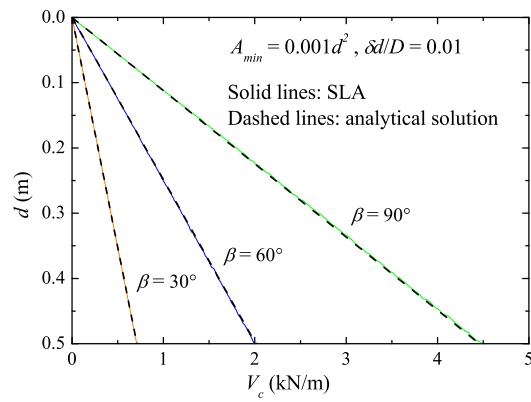


Figure 15. Indentation resistance for different wedge angles.

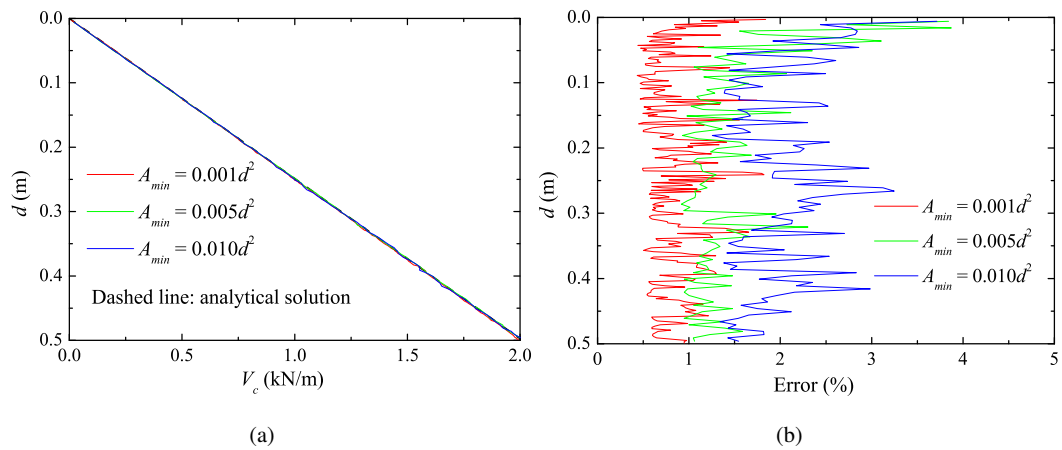


Figure 16. Influence of minimum element size A_{min} on wedge indentation response: (a) resistance; (b) normalised bracketing discrepancy. $\beta = 60^\circ$ and $\delta d/D = 0.01$.

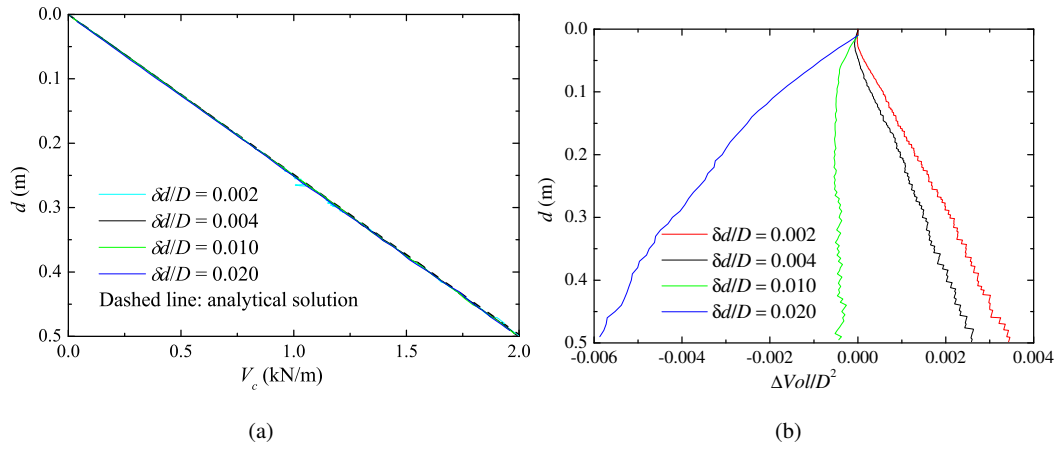


Figure 17. Influence of displacement increment δd on wedge indentation response: (a) resistance; (b) normalised volume change. $\beta = 60^\circ$ and $A_{min} = 0.001d^2$.

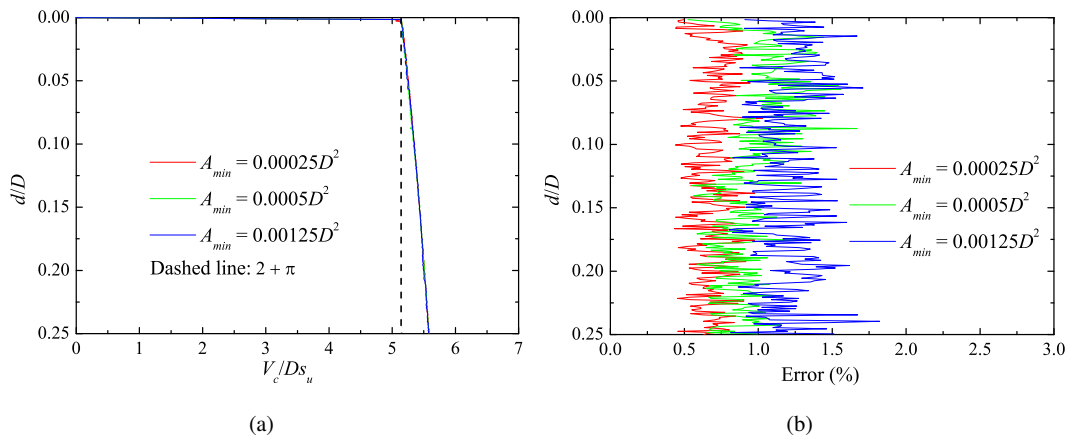


Figure 18. Influence of minimum element size A_{min} on strip footing indentation response: (a) normalised resistance; (b) normalised bracketing discrepancy. $\delta d/D = 0.001$.

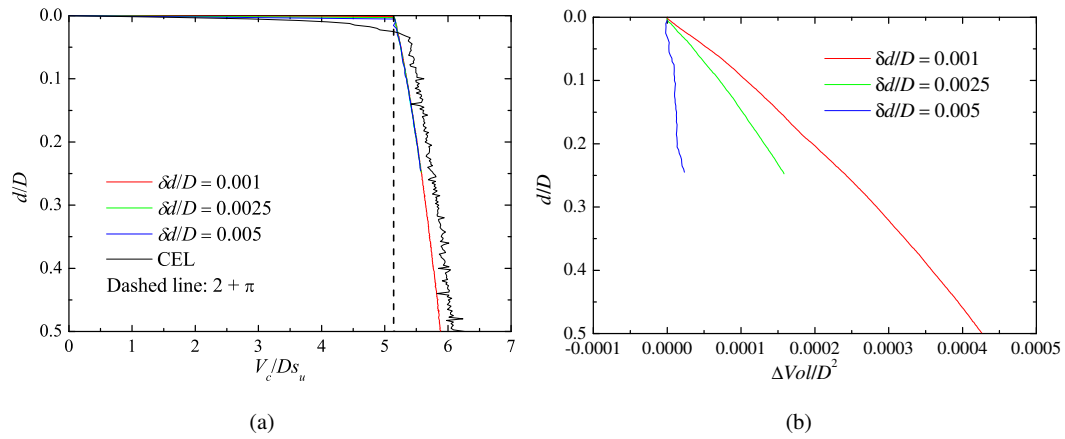


Figure 19. Influence of displacement increment δd on strip footing indentation response: (a) normalised resistance; (b) normalised volume change. $A_{min} = 0.00025D^2$.

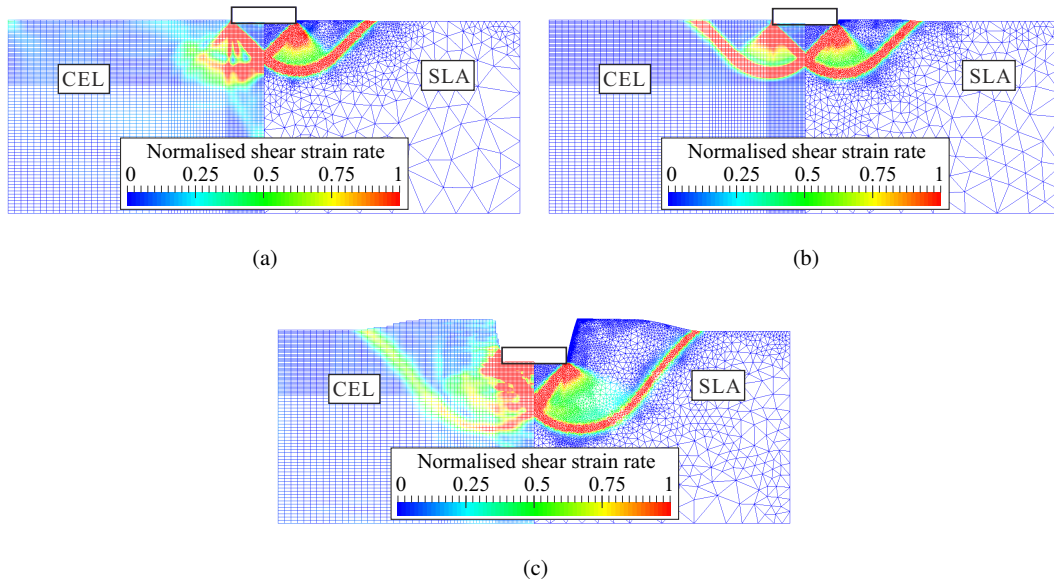


Figure 20. Soil failure mechanisms (contours of $\dot{\gamma}D/v_p$) for strip footing: (a) $d/D = 0.03$; (b) $d/D = 0.05$; (c) $d/D = 0.5$.

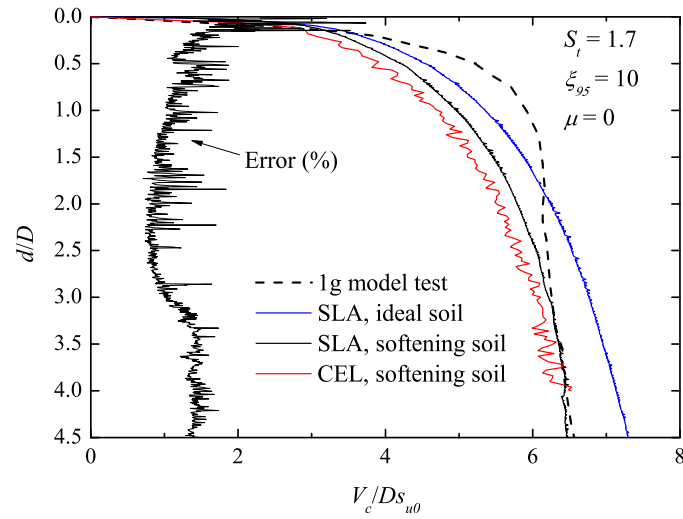


Figure 21. Indentation response of pipe (deep penetration): normalised resistance, also showing normalised bracketing discrepancy for SLA with softening soil.

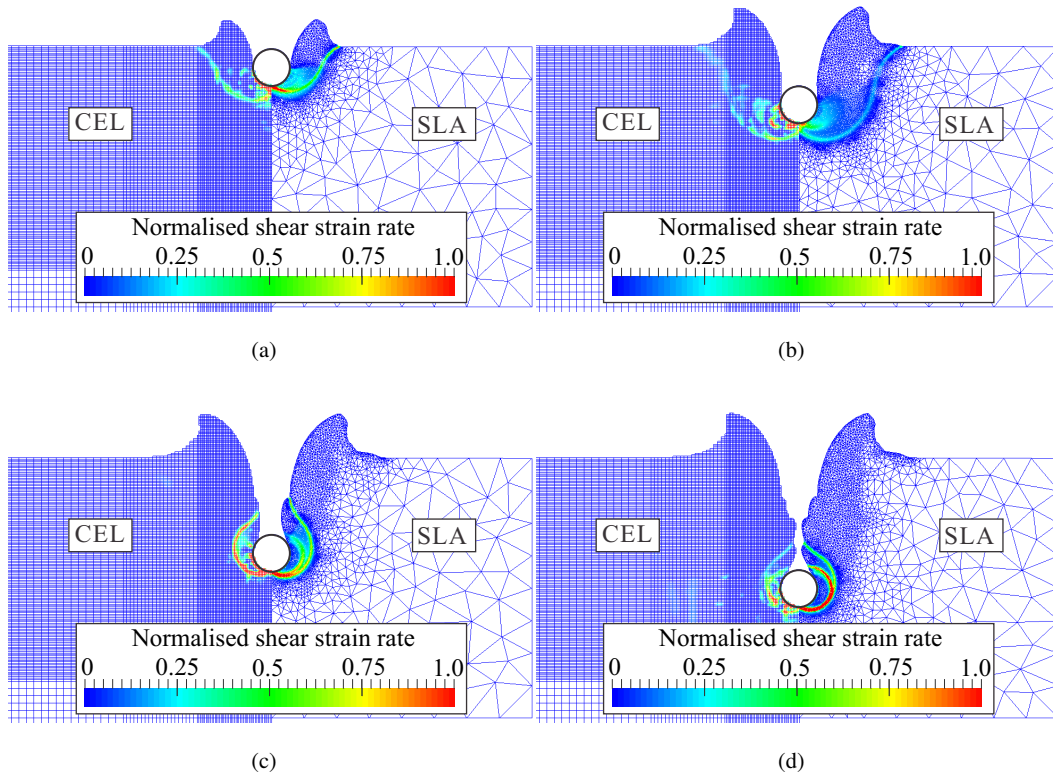


Figure 22. Soil failure mechanisms (contours of $\dot{\gamma}D/v_p$) for pipe (deep penetration): (a) $d/D = 1$; (b) $d/D = 2$; (c) $d/D = 3$; (d) $d/D = 4$.

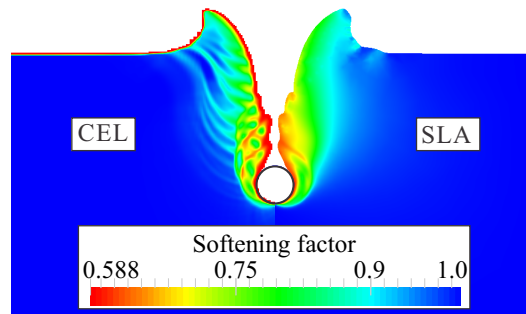


Figure 23. Softening factor for soil strength at end of deep pipe penetration ($d/D = 4$).

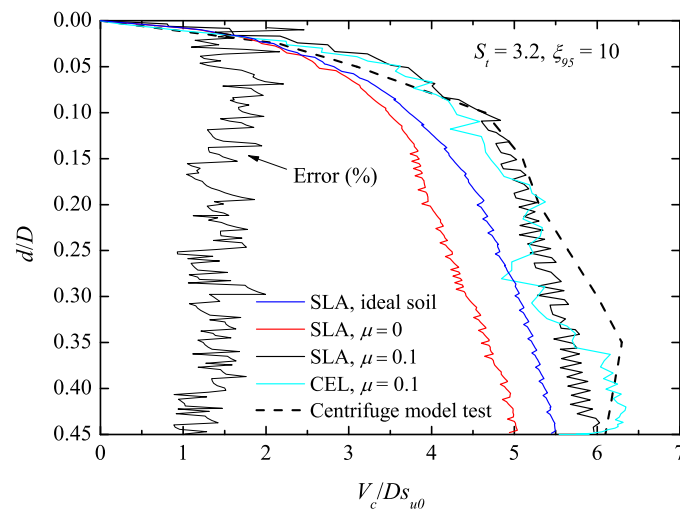


Figure 24. Indentation response of pipe (shallow penetration): normalised resistance, also showing normalised bracketing discrepancy for SLA with $\mu = 0.1$.

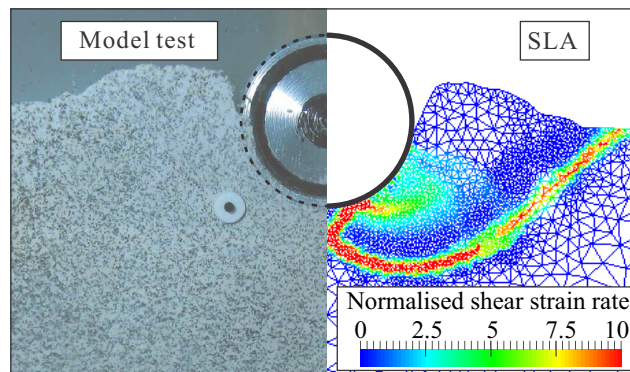


Figure 25. Soil failure mechanism (contours of $\dot{\gamma}D/v_p$) at end of shallow pipe penetration ($d/D = 0.45$).

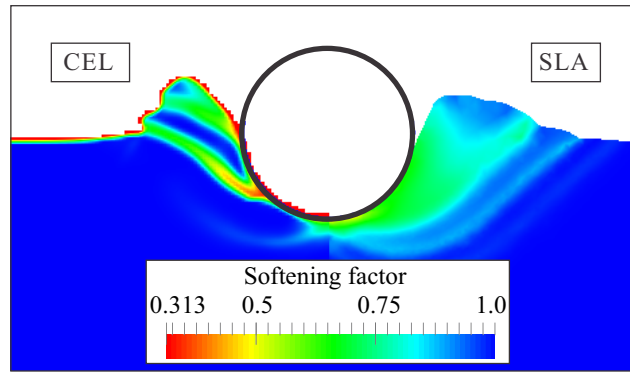


Figure 26. Softening factor for soil strength at end of shallow pipe penetration ($d/D = 0.45$).

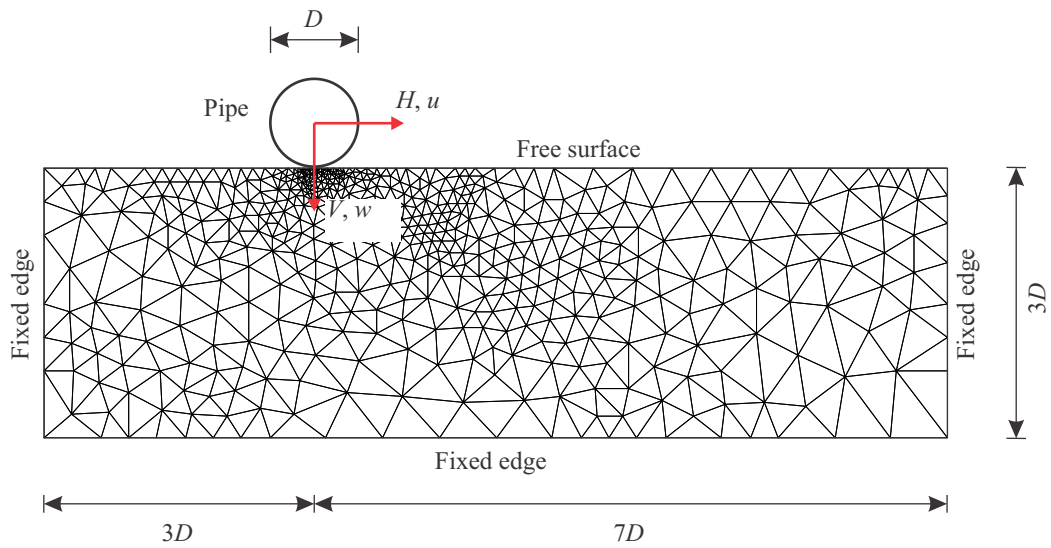


Figure 27. Initial configuration of SLA model for indentation and lateral loading of a pipe.

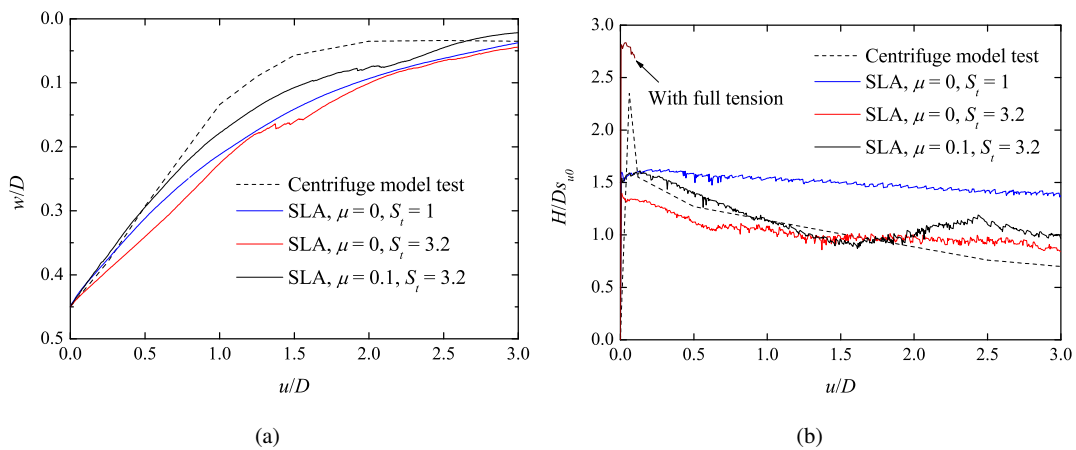


Figure 28. Lateral loading response of pipe: (a) invert trajectory; and (b) normalised lateral resistance.

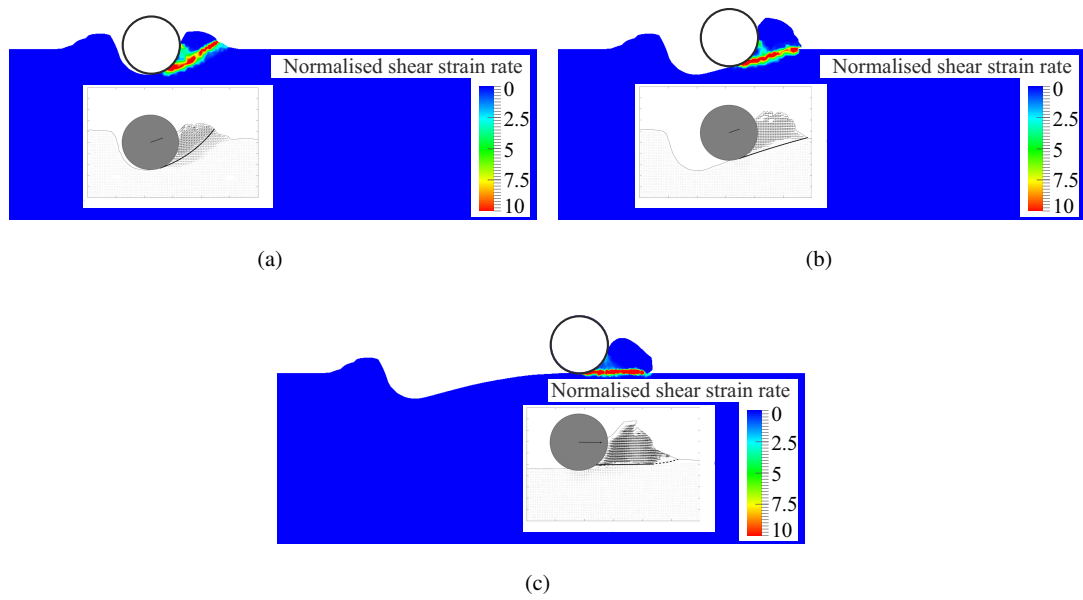


Figure 29. Soil failure mechanisms (contours of $\dot{\gamma}D/v_p$) during lateral loading of pipe: (a) $u/D = 0.1$; (b) $u/D = 0.6$; (c) $u/D = 2.9$.

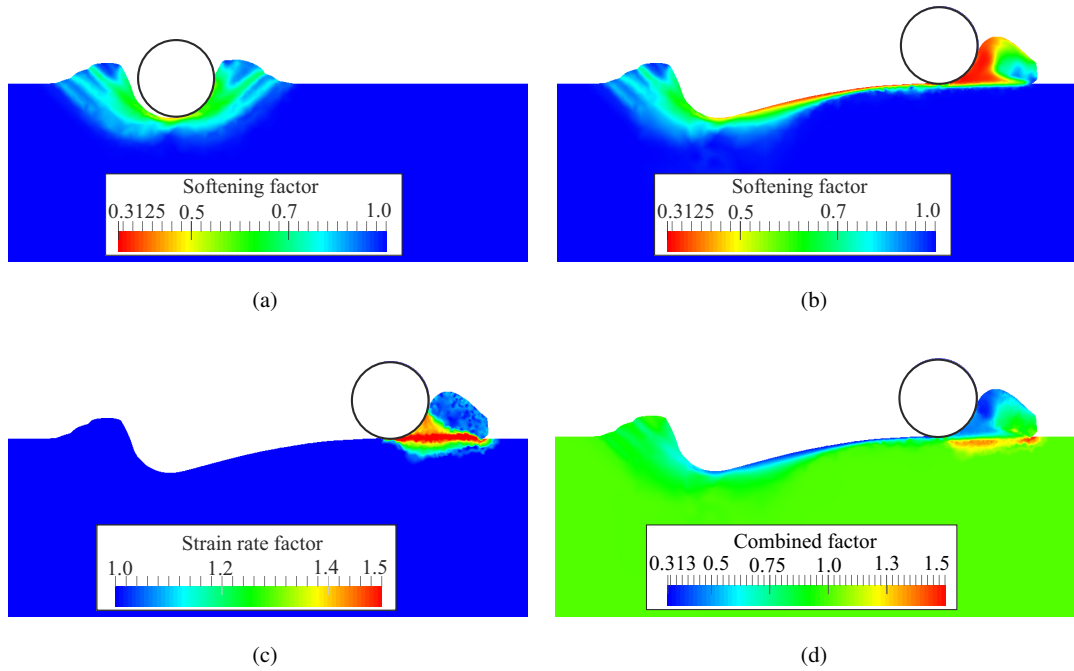


Figure 30. Softening and strain rate factors for soil strength during lateral loading of pipe: (a) softening factor at $u/D = 0.1$; (b) softening factor at $u/D = 2.9$; (c) strain rate factor at $u/D = 2.9$; (d) combined factor at $u/D = 2.9$.

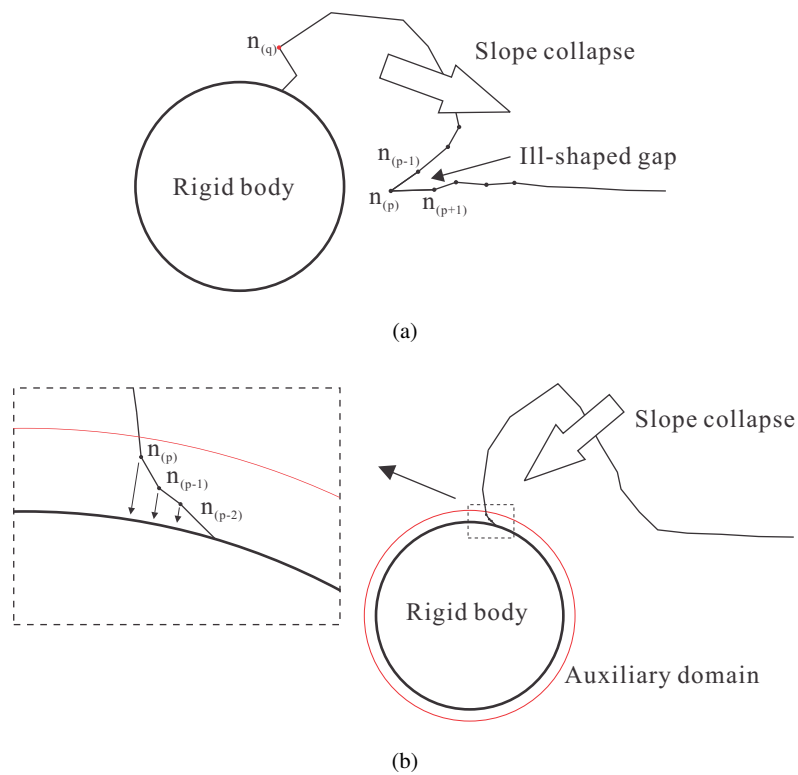


Figure 31. Conditions that may cause slope instability: (a) an ill-shaped gap; (b) a steep slope above the rigid body.